Science Advances

AAAS

Supplementary Materials for

Robust, high-performance n-type organic semiconductors

Toshihiro Okamoto*, Shohei Kumagai, Eiji Fukuzaki, Hiroyuki Ishii, Go Watanabe, Naoyuki Niitsu, Tatsuro Annaka, Masakazu Yamagishi, Yukio Tani, Hiroki Sugiura, Tetsuya Watanabe, Shun Watanabe, Jun Takeya

*Corresponding author. Email: tokamoto@k.u-tokyo.ac.jp

The PDF file includes:

> Sections S1 to S9
> Figs. S1 to S31
> Tables S1 to S6
> Legends for movies S1 to S4
> References

Other Supplementary Material for this manuscript includes the following:

(available at advances.sciencemag.org/cgi/content/full/6/18/eaaz0632/DC1)

> Movies S1 to S4

Section S1. Details of syntheses and characterizations

<u>Reagents and Starting Materials</u>

1,5-Dinitroanthraquinone, methyl cyanoacetate, potassium t-butoxide (KO^{t}Bu), 1,3-dimethyl-2-imidazolidinone (DMI), sulfuric acid (H$_2$SO$_4$), 4-dimethylaminopyridine (DMAP), N-phenylbis(trifluoromethanesulfonimide) (Tf$_2$NPh), formic acid, tetrakis(triphenylphophine)palladium (0) (Pd(PPh$_3$)$_4$), N-bromosuccinimide (NBS), 2,4,6-trichlorophenyl formate, palladium acetate (Pd(OAc)$_2$), 4,5-bis(diphenylphosphino)-9,9-dimethylxanthene (Xantphos), p-toluenesulfonic acid monohydrate (p-TsOH$\cdot$H$_2$O), propionic acid, 2-phenylethylamine, octylamine, 4-heptylamine, perylene-3,4,9,10-tetracarboxylic dianhydride were purchased from either Tokyo Chemical Industry Co., Ltd, Sigma-Aldrich Inc., KANTO chemical Co., Ltd., or Fujifilm-Wako Pure Chemical Industries, Ltd. Nuclear magnetic resonance (NMR) spectra were recorded with chloroform-D (CDCl$_3$) (D, 99.8%) containing 0.05% (v/v) tetramethylsilane (TMS) or 1,1,2,2-tetrachloroethane-d_2 (CDCl$_2$CDCl$_2$) (D, 99.5%) purchased from Cambridge Isotope Laboratries, Inc.

<u>Methods</u>

All the reactions were carried out under argon, and air- or moisture-sensitive liquids and solutions were transferred via a syringe or a Teflon cannula. Analytical thin-layer chromatography (TLC) was performed on glass plates coated with a 0.25 mm-thick layer of 230–400 mesh silica gel containing a fluorescent indicator (Merck silica gel 60 F254). TLC plates were visualized by exposure to an ultraviolet lamp (254 or 365 nm) and by immersion in 10% phosphomolybdic acid in ethanol followed by heating on a hot plate. Flash column chromatography was performed on Kanto silica gel 60 and open column chromatography was performed on Wakogel C-200 (75–150 μm). Melting points (mp) were collected on a Mettler Toledo MP70 Melting Point System. ^{1}H and ^{13}C NMR spectra were measured with a JEOL ECS400 spectrometer (400 MHz for ^{1}H and 100 MHz for ^{13}C) in CDCl$_3$ at room temperature or CDCl$_2$CDCl$_2$ at 100 °C. Chemical shifts are reported in δ ppm. ^{1}H NMR and ^{13}C NMR spectra are referenced to residual protons (δ 7.26 ppm for chloroform, 5.93 ppm for 1,1,2,2-tetrachloroethane (TCE)) and carbon-13 in the deuterated solvent (δ 77.16 ppm for chloroform, 74.00 ppm for TCE) as an internal standard, respectively. The data are presented in the following format: chemical shift, multiplicity (s = singlet, d = doublet, t = triplet, q = quartet, m = multiplet), coupling constant in Hertz (Hz), signal area integration in natural numbers. Recycling preparative gel permeation chromatography (GPC) was performed with a Japan Analytical Industry (JAI) LC-918 equipped with polystyrene gel columns (JAIGEL 1H and 2H) using chloroform as an eluent. Time-of-flight high-resolution mass (TOF-MS) spectrometry was performed with a Thermo Fisher LTQ-Orbitrap XL with the atmospheric pressure chemical ionization (APCI) method at Comprehensive Analysis Center, The Institute of Scientific and Industrial Research, Osaka University. Elemental analysis was carried out on a J-Science Lab JM10 CHN analyzer at Comprehensive Analysis Center, the Institute of Scientific and Industrial Research, Osaka University or on an Elementar vario MICRO cube at The Microanalytical Laboratory, Department of Chemistry, Graduate School of Science, The University of Tokyo.
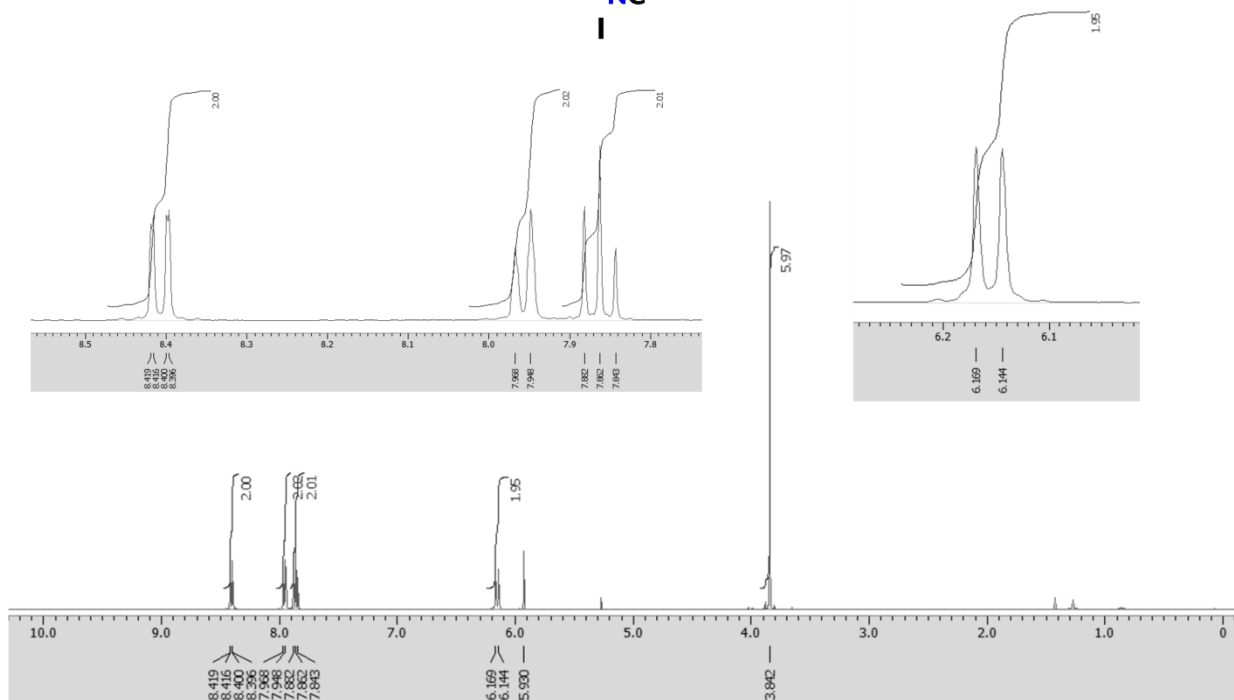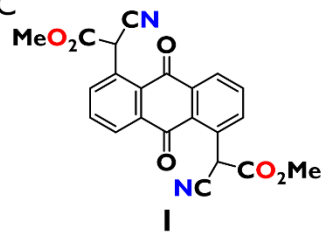
Fig. S1. ^{1}H NMR spectrum of **1** (CDCl$_2$CDCl$_2$, 100 °C)

¹³C, 100MHz, CDCl$_2$CDCl$_2$, 100 °C
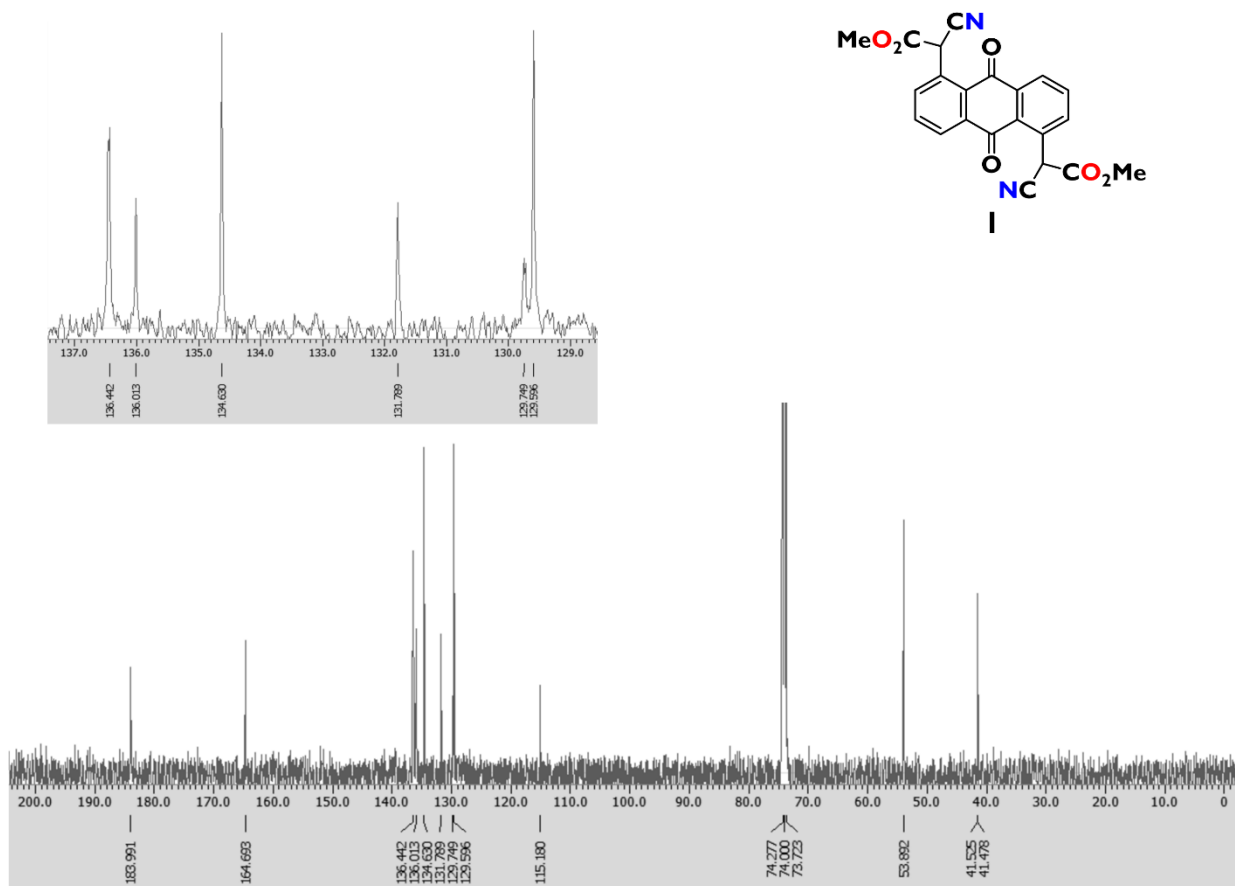
Fig. S2. ¹³C NMR spectrum of compound 1 (CDCl₂CDCl₂, 100 °C)

¹H, 400MHz, CDCl₂CDCl₂, 100 °C
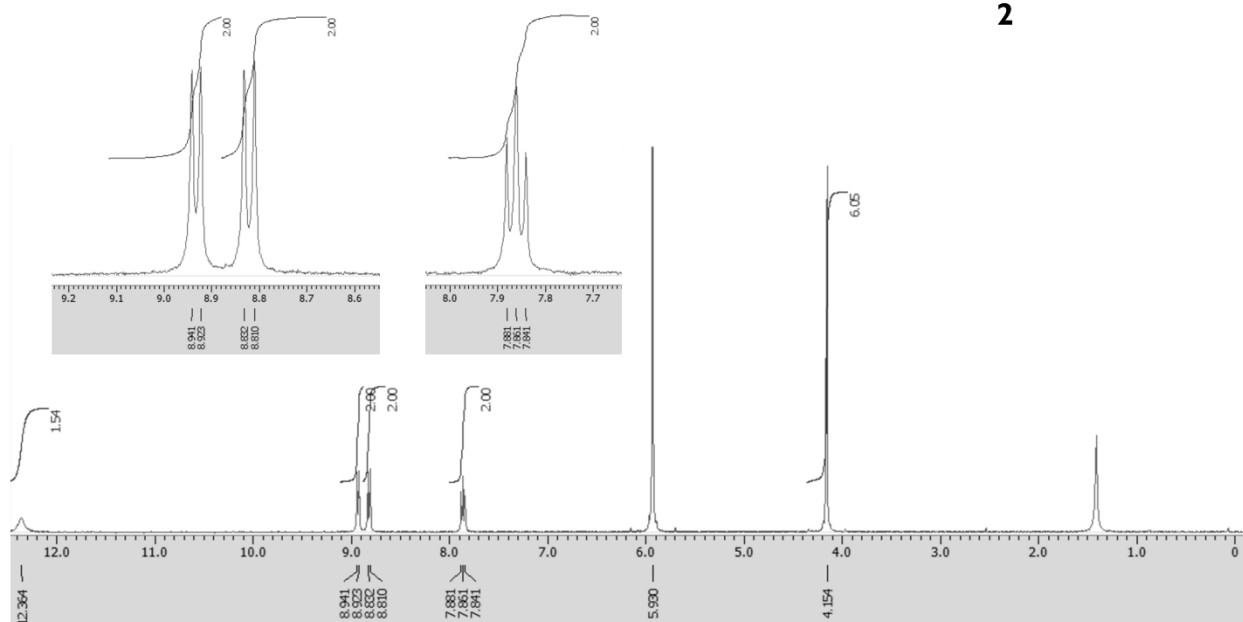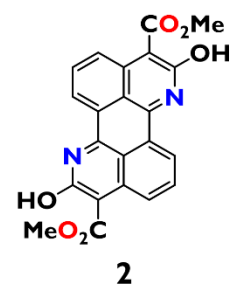
Fig. S3. ¹H NMR spectrum of compound 2 (CDCl₂CDCl₂, 100 °C)

$^{13}C, 100MHz, CDCl_2CDCl_2, 100\ ^\circ C$
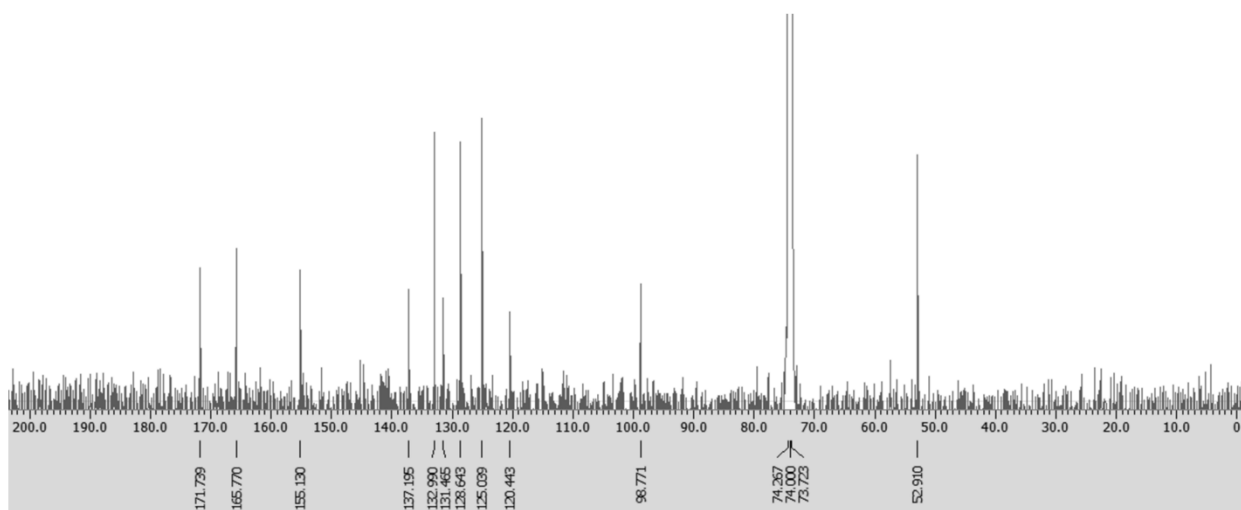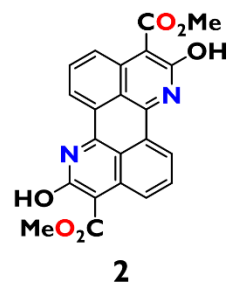
Fig. S4. ^{13}C NMR spectrum of compound 2 (CDCl₂CDCl₂, 100 °C)

¹H, 400MHz, CDCl₂CDCl₂, 100 °C
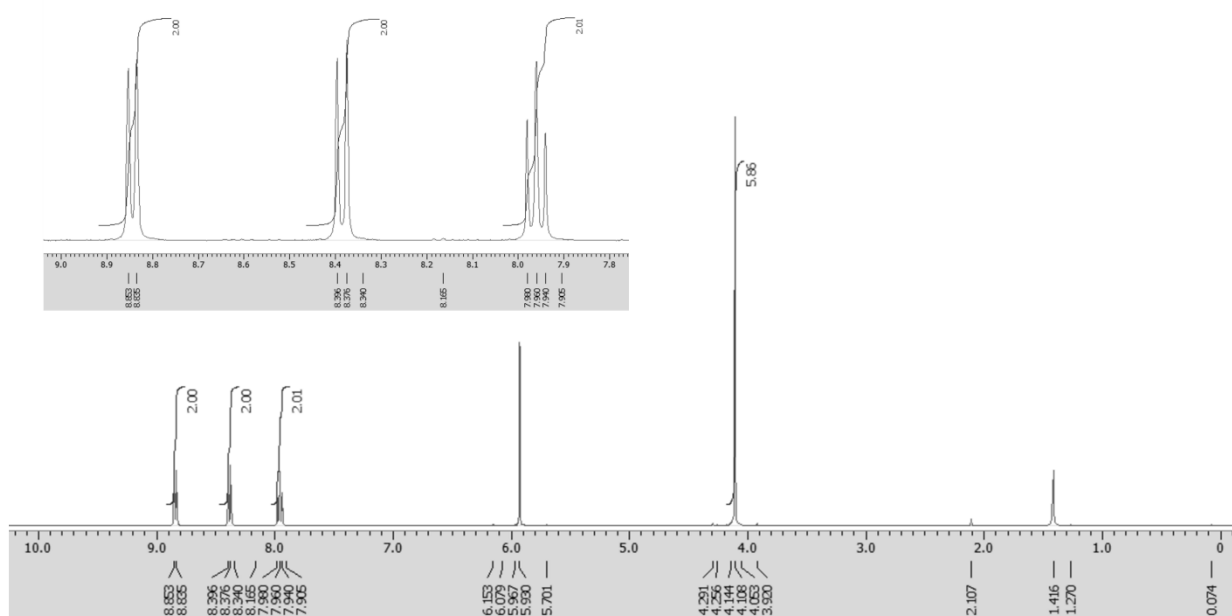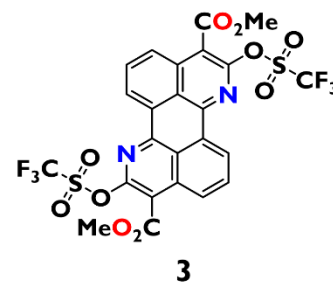
Fig. S5. ¹H NMR spectrum of compound 3 (CDCl₂CDCl₂, 100 °C)

^{13}C, 100MHz, CDCl$_2$CDCl$_2$, 100 °C
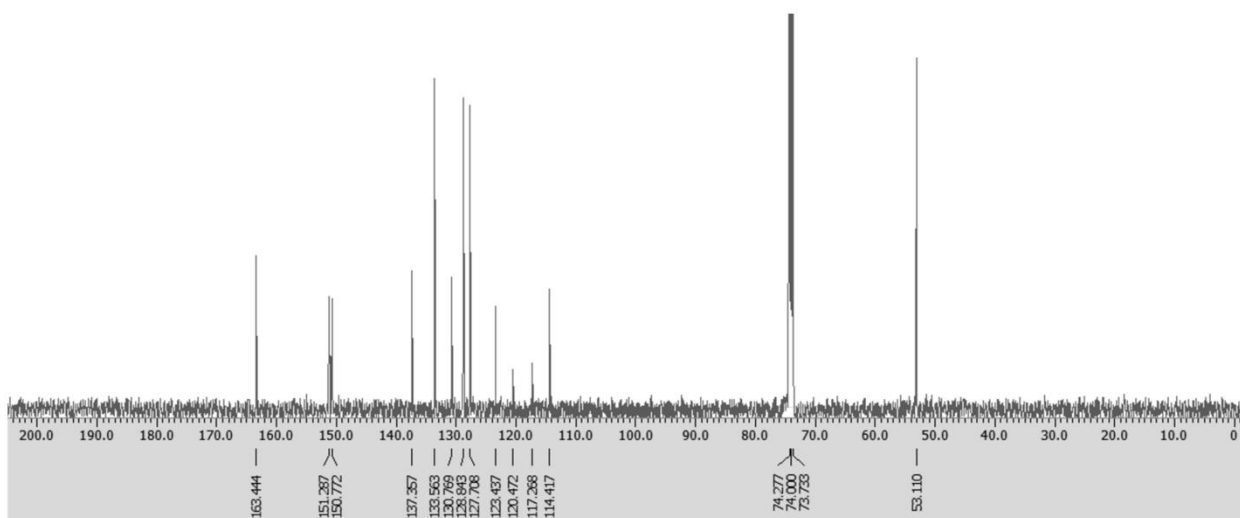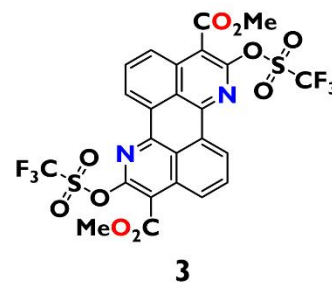
Fig. S6. ^{13}C NMR spectrum of compound 3 (CDCl₂CDCl₂, 100 °C)

¹H, 400MHz, CDCl₂CDCl₂, 100 °C
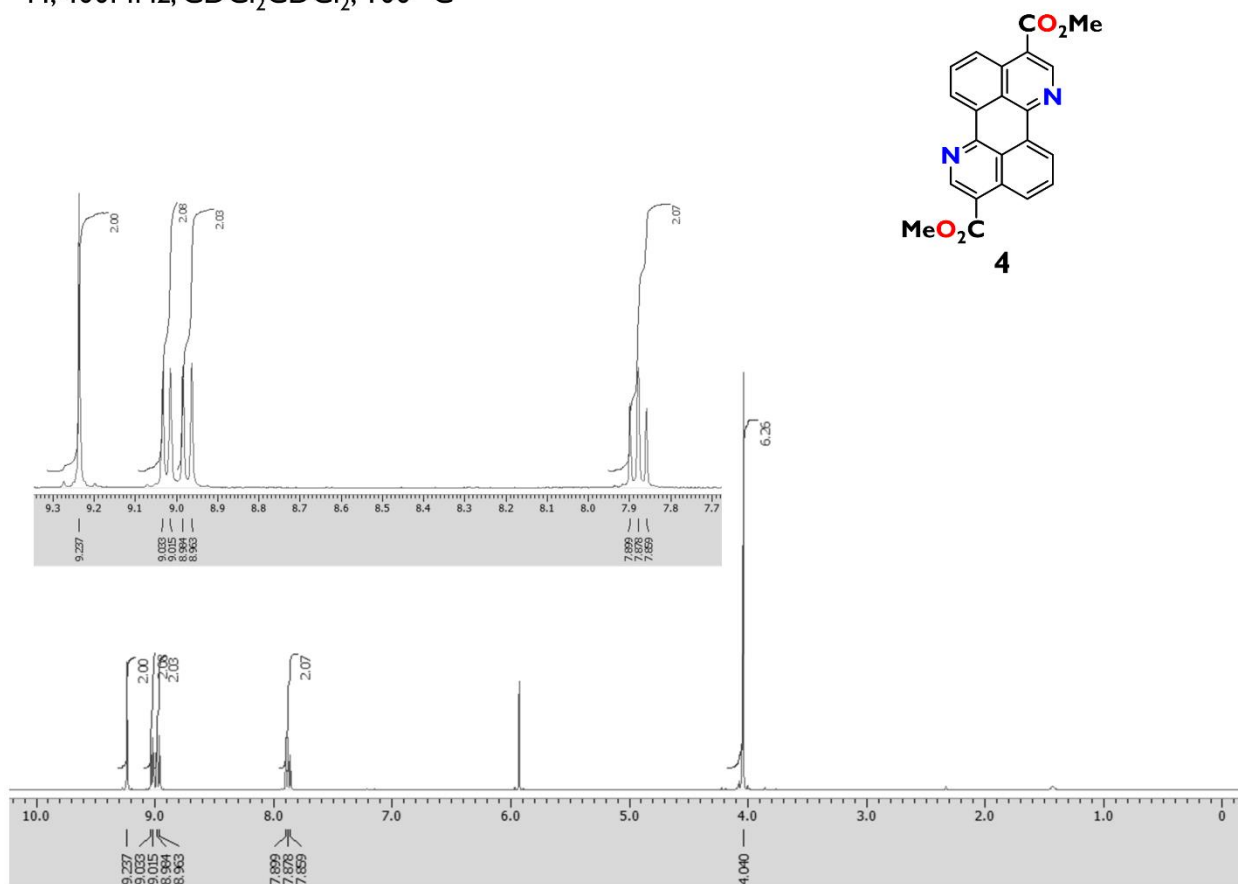
Fig. S7. ¹H NMR spectrum of compound 4 (CDCl₂CDCl₂, 100 °C)

^{13}C, 100MHz, CDCl$_2$CDCl$_2$, 100 °C
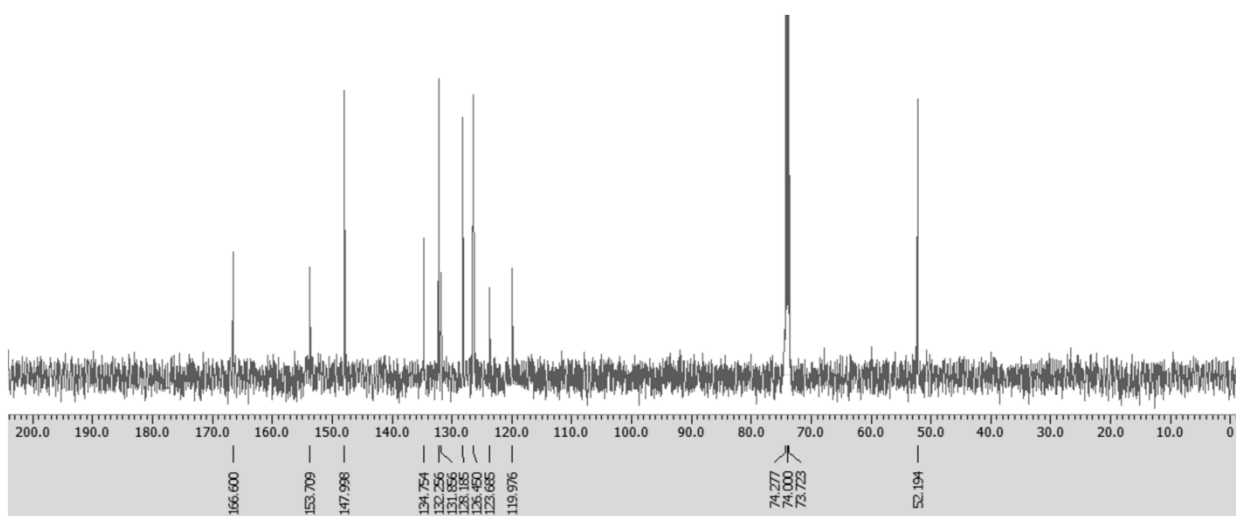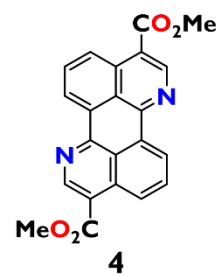
Fig. S8. ^{13}C NMR spectrum of compound 4 (CDCl$_2$CDCl$_2$, 100 °C)
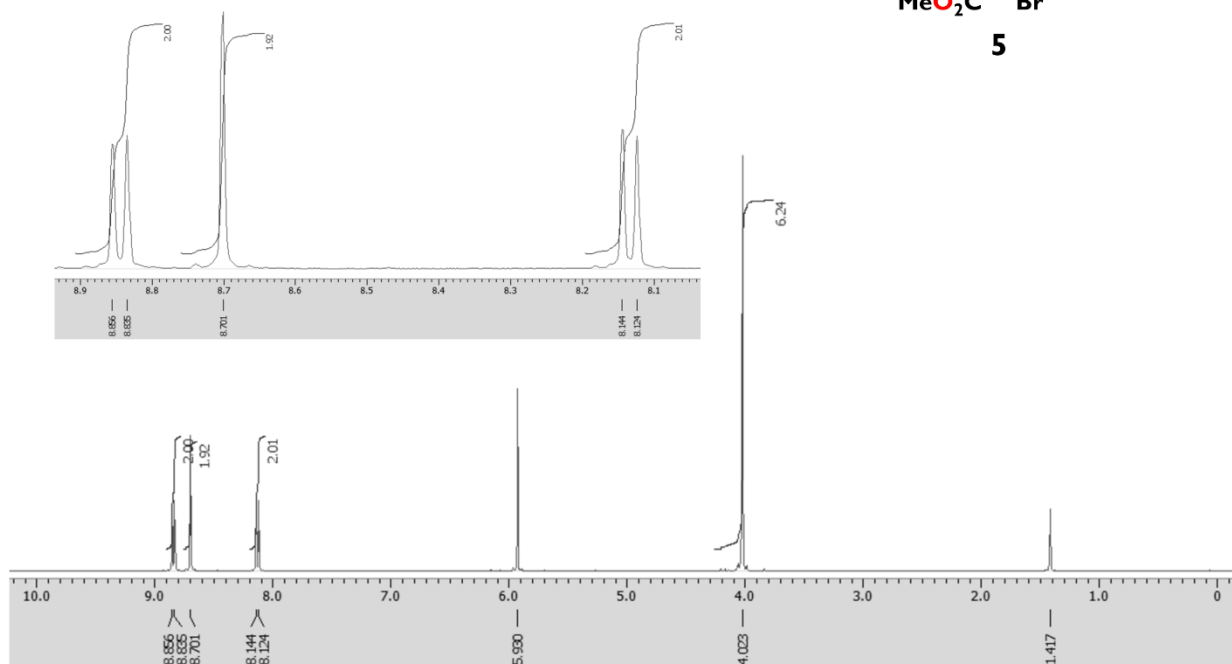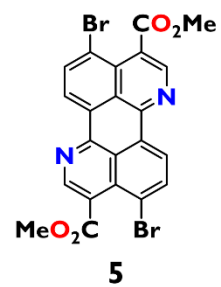
¹H, 400MHz, CDCl₂CDCl₂, 100 °C

Fig. S9. ¹H NMR spectrum of compound 5 (CDCl₂CDCl₂, 100 °C)
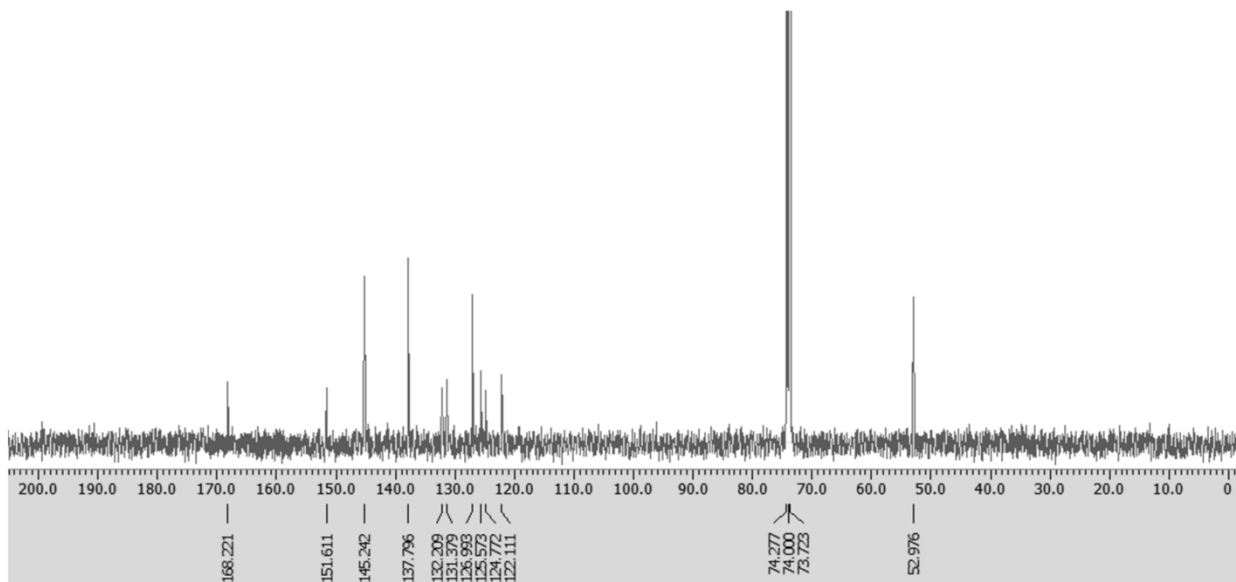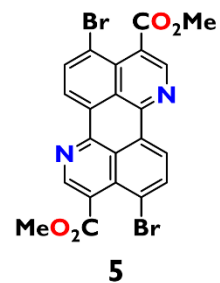
Fig. S10. ^{13}C NMR spectrum of compound 5 (CDCl$_2$CDCl$_2$, 100 °C)

¹H, 400MHz, CDCl₂CDCl₂, 100 °C
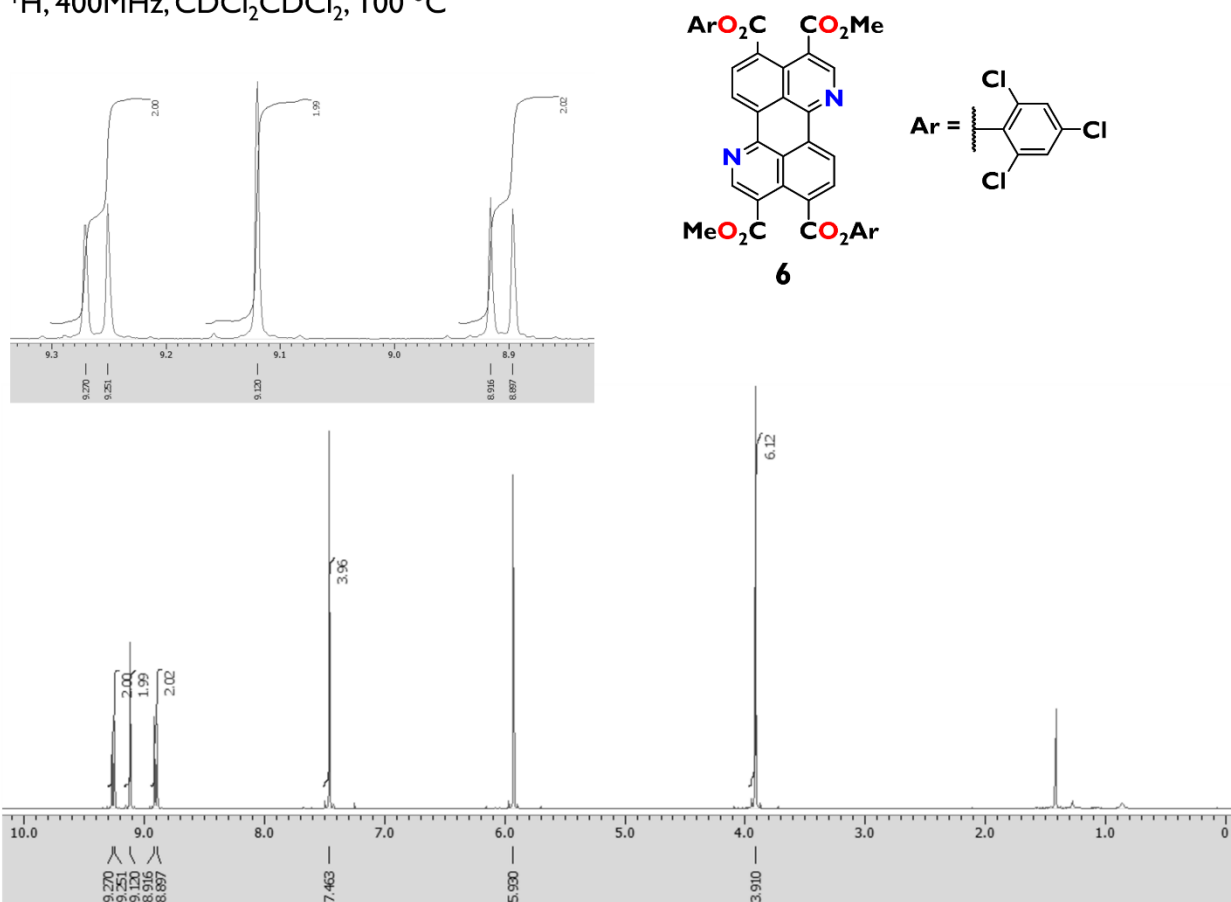
Fig. S11. ¹H NMR spectrum of compound 6 (CDCl₂CDCl₂, 100 °C)

¹³C, 100MHz, CDCl₂CDCl₂, 100 °C
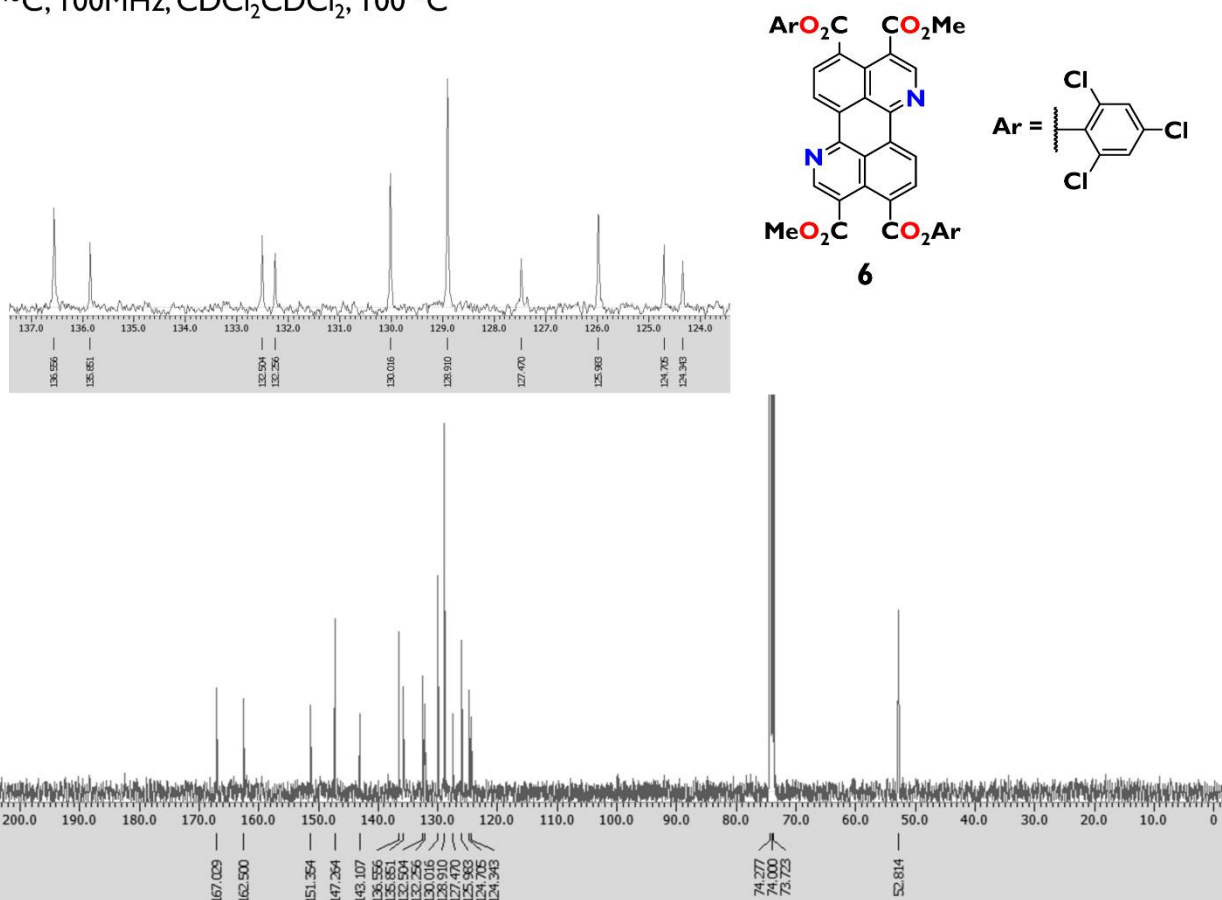
Fig. S12. ¹³C NMR spectrum of compound **6** (CDCl₂CDCl₂, 100 °C)

^{1}H, 400MHz, CDCl$_2$CDCl$_2$, 100 °C
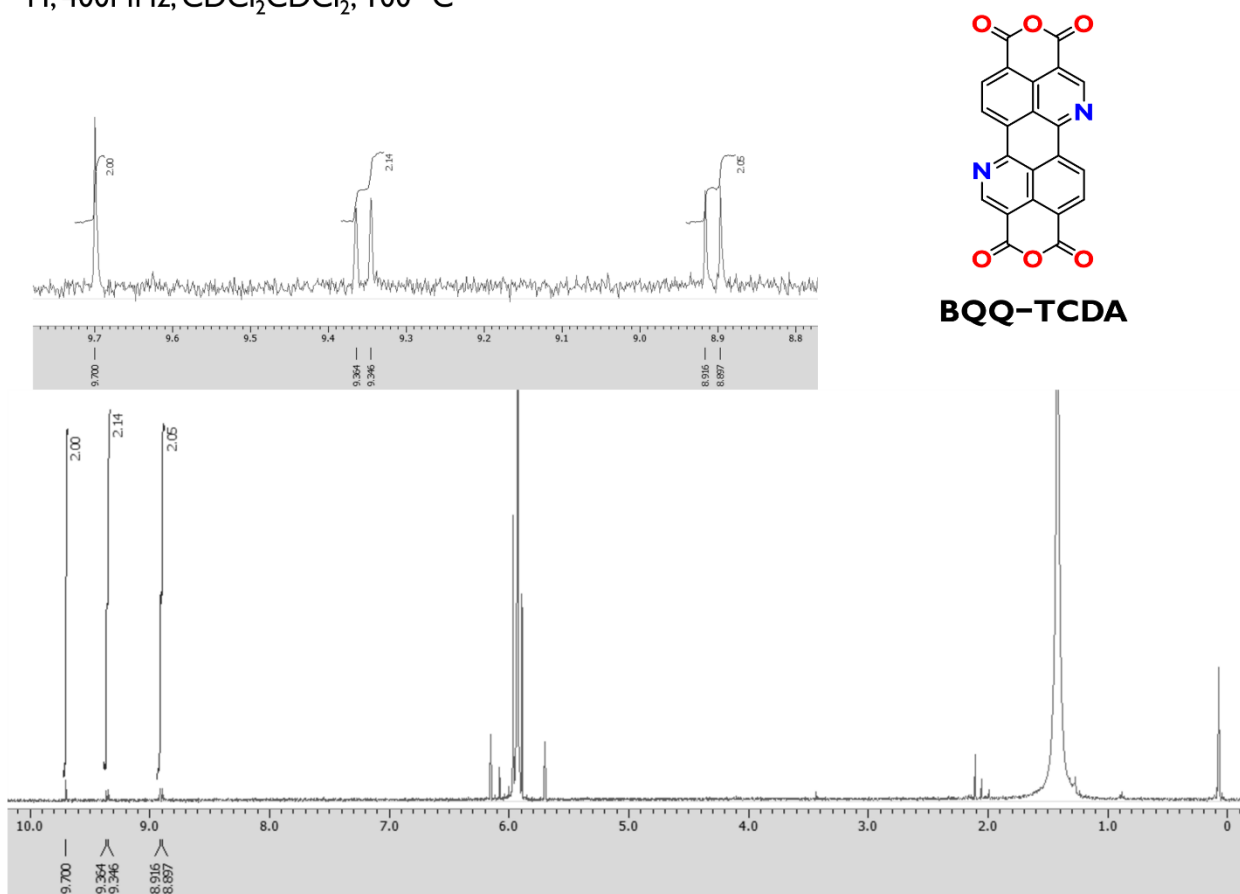
Fig. S13. ^{1}H NMR spectrum of BQQ−TCDA (CDCl$_2$CDCl$_2$, 100 °C)

¹H, 400MHz, CDCl$_2$CDCl$_2$, 100 °C
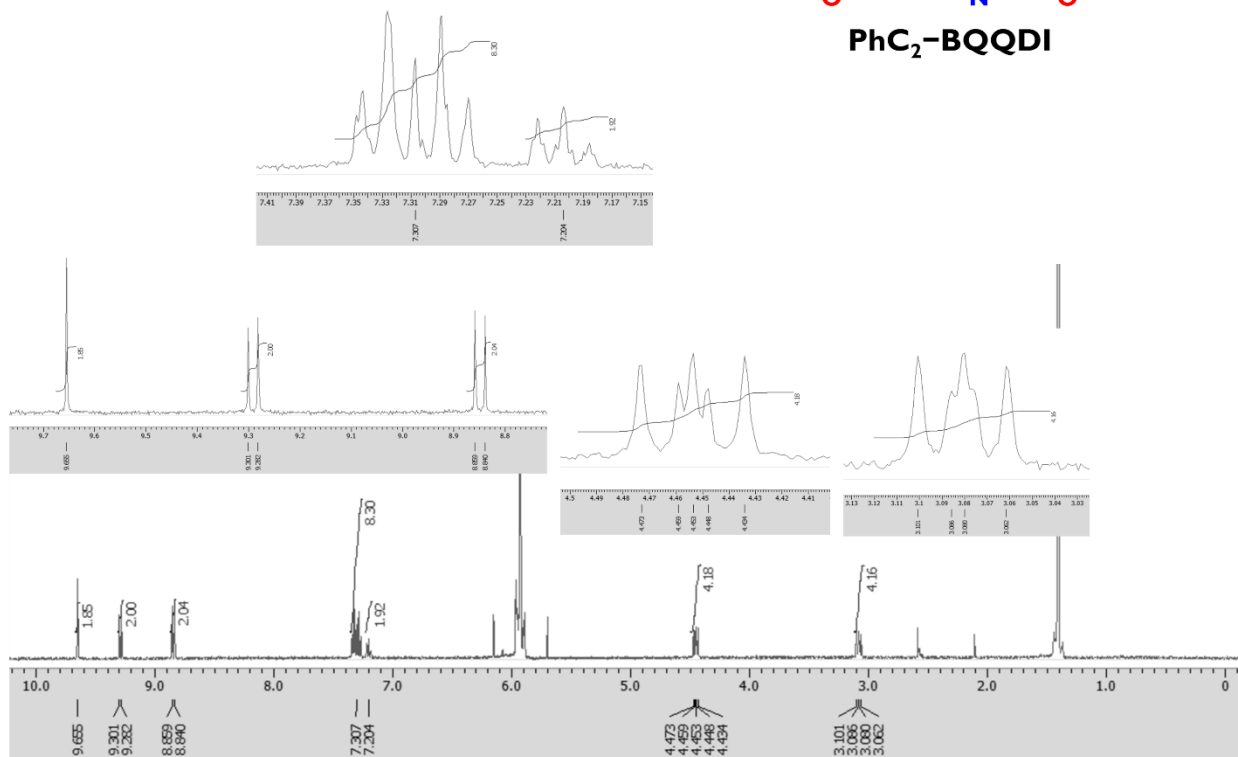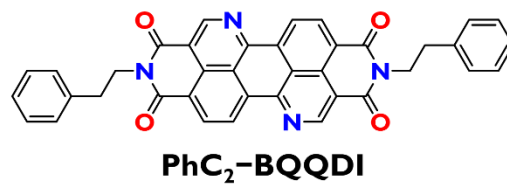
Fig. S14. ¹H NMR spectrum of PhC$_2$−BQQDI (CDCl$_2$CDCl$_2$, 100 °C)

¹H, 400MHz, CDCl₂CDCl₂, 100 °C
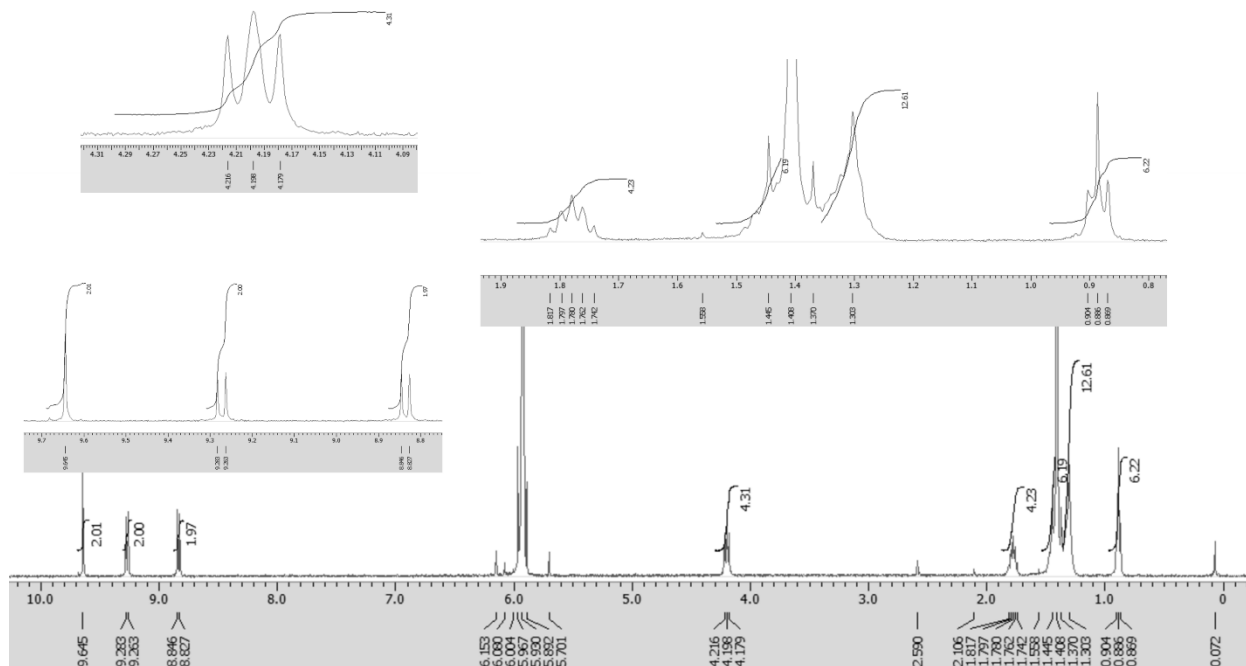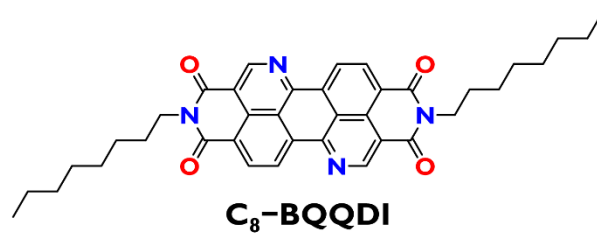
C₈−BQQDI

Fig. S15. ¹H NMR spectrum of C₈−BQQDI (CDCl₂CDCl₂, 100 °C)

¹H, 400MHz, CDCl₃, 30 °C
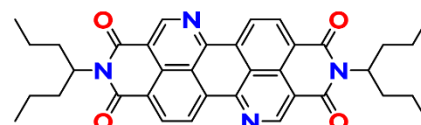
4-Hep−BQQDI
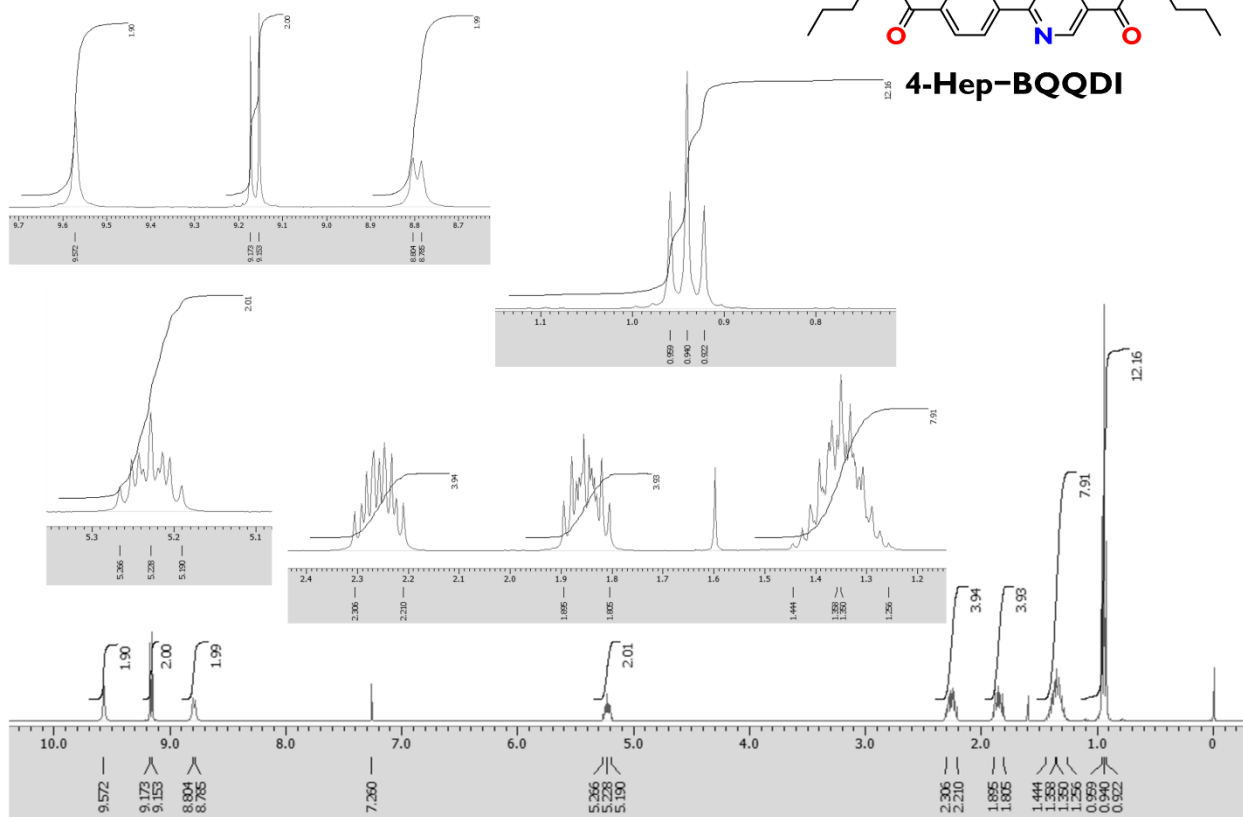
Fig. S16. ¹H NMR spectrum of 4-Hep−BQQDI (CDCl₃, 30 °C)

19

^{13}C, 100MHz, $CDCl_3$, 30 °C
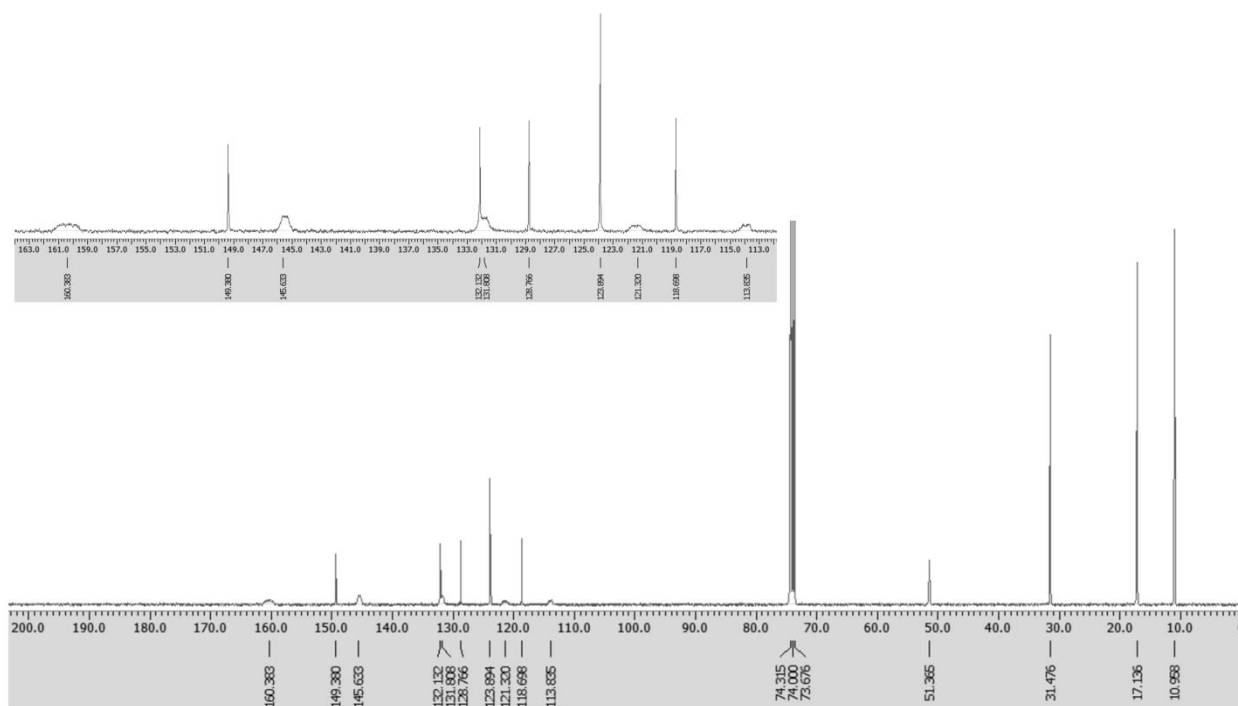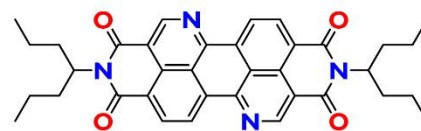
Fig. S17. ^{13}C NMR spectrum of 4-Hep−BQQDI ($CDCl_3$, 30 °C)

<u>General Synthesis of PDI Derivatives (R = PhC$_2$, C$_8$ and 4-Hep)</u>

R−PDI derivatives were synthesized in the same manner as **BQQDI** derivatives. A mixture of perylene-3,4,9,10-tetracarboxylic dianhydride and respective amine (2.4 equiv.) in quinoline (0.025 M) was heated at 160 °C for 3−22 h. After cooling to room temperature, an excess amount of MeOH was added to the reaction mixture to obtain the crude precipitates which were collected by filtration to afford the desired compounds. Further purifications were performed by sublimation or column chromatography.

N,N-Diphenethyl-3,4,9,10-perylenetetracarboxylic acid diimide (PhC$_2$–PDI)
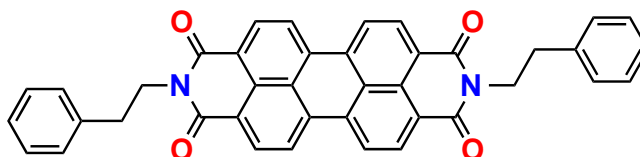
PhC$_2$–PDI

Reaction period was 16 h. Crude yield 98%. Purification was carried out by sublimation. Purification yield: 78% (dark-brown solid). m.p.: >350 °C. ^{1}H NMR (400 MHz, CDCl$_2$CDCl$_2$ at 100 °C): δ 8.68 (d, J = 8.0 Hz, 4H), 8.62 (d, J = 8.4 Hz, 4H), 7.36–7.27 (m, 8H), 7.20 (td, J = 7.2 Hz, J = 4.0 Hz, 2H), 4.44 (td, J = 7.6 Hz, J = 4.8 Hz, 4H), 3.07 (t, J = 7.8 Hz, 4H). Anal. Calcd for C$_{40}$H$_{26}$N$_2$O$_4$: C, 80.25; H, 4.38; N, 4.68, found: C, 80.48; H, 4.51; N, 4.74.

N,N-Dioctyl-3,4,9,10-perylenetetracarboxylic acid diimide (C$_8$–PDI)
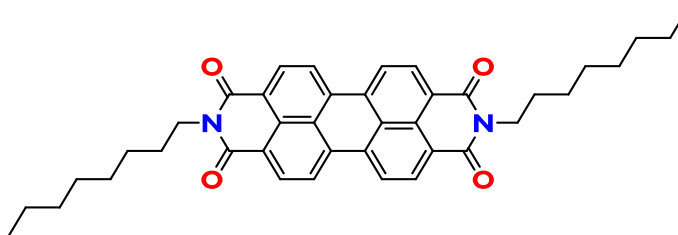
C$_8$–PDI

Reaction period was 3 h. Crude yield 96%. Purification was carried out by sublimation. Purification yield: 86% (brown solid). ^{1}H NMR (400 MHz, CDCl$_3$ at 40 °C): δ 8.70 (d, J = 8.0 Hz, 4H), 8.63 (d, J = 8.0 Hz, 4H), 4.21 (t, J = 7.6 Hz, 4H), 1.77 (m, 4H), 1.48−1.26 (m, 20H), 0.88 (t, J = 7.0 Hz, 6H). Anal. Calcd for C$_{40}$H$_{42}$N$_2$O$_4$: C, 78.15; H, 6.89; N, 4.56, found: C, 78.17; H, 6.96; N, 4.63. Plate-shaped red single crystals of **C$_8$−PDI** were grown by recrystallization from nitrobenzene under ambient atmosphere. The single crystal obtained was measured at 298 K. A total of 6423 reflections were measured at the maximum 2θ angle of

75.786°, of which 3359 were independent reflections (R_{int} = 0.0190). The analysis was carried out with space group of $P\bar{1}$ without disorder expediently. The crystal data are as follows: $C_{40}H_{42}N_2O_4$; FW = 614.76, Triclinic, $P\bar{1}$, a = 4.7647(2) Å, b = 8.5099(3) Å, c = 20.2613(6) Å, α = 85.332(2)°, β = 89.683(2)°, γ = 82.285(3)°, V = 811.39(5) Å^3, Z = 1, D_{calcd} = 1.258 g cm^{-3}, $F(000)$ = 328.0, μ = 0.639 (mm^{-1}), the refinement converged to R_1 [$I>2\sigma(I)$] = 0.0514, wR_2 (all data) = 0.1594, GOF = 1.089 (CCDC-1938482).

N,N-Di(4-heptyl)-3,4,9,10-perylenetetracarboxylic acid diimide (4-Hep−PDI)(*61*)
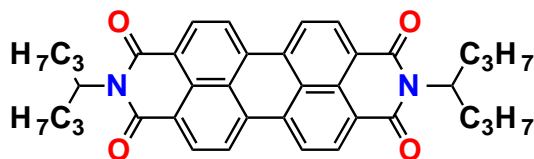
4-Hep–PDI

Reaction period was 22 h. Purification was carried out by silica-gel column chromatography (CHCl$_3$−acetone (99:1)). Yield: 61% (red solid). ^{1}H NMR (400 MHz, CDCl$_3$ at 40 °C): δ 8.69−8.61 (m, 4H), 5.28−5.20 (m, 2H), 2.32−2.22 (m, 4H), 1.88−1.78 (m, 4H), 1.43−1.23 (m, 8H), 0.93 (t, J = 7.4 Hz, 6H). Anal. Calcd for $C_{38}H_{38}N_2O_4$: C, 77.79; H, 6.53; N, 4.77, found: C, 77.70; H, 6.54; N, 4.73.

A mixture of 2,9-Bis(2,2,3,3,4,4,4-heptafluorobutyl)-1,2,3,8,9,10-hexahydro-1,3,8,10-tetraoxoanthra[2,1,9-*def*:6,5,10-*d'e'f'*]diisoquinoline-5,12-dicarbonitrile (PDI−FCN$_2$ [5,12-]) and 2,9-Bis(2,2,3,3,4,4,4-heptafluorobutyl)-1,2,3,8,9,10-hexahydro-1,3,8,10-tetraoxoanthra[2,1,9-*def*:6,5,10-*d'e'f'*]diisoquinoline-5,13-dicarbonitrile (PDI−FCN$_2$ [5,13-])
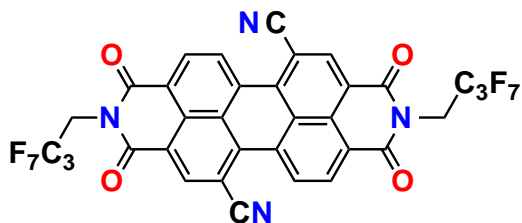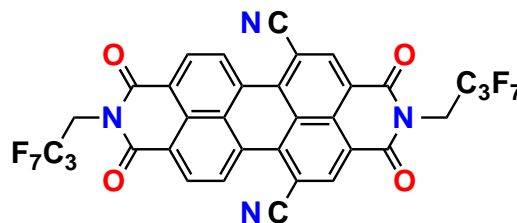
PDI–FCN$_2$ (5,12-)   **PDI–FCN$_2$ (5,13-)**

PDI−FCN$_2$ was synthesized according to the literature(*30*). Since **PDI−FCN$_2$** was composed of two CN–substituted isomers at 5,12- and 5,13-positions due to the synthetic issue, their ratio was determined by ^{1}H NMR to be [5,12] : [5,13] ≈ 0.83 : 0.17. Dark-brown solid after sublimation. ^{1}H NMR (400 MHz, CDCl$_3$ at r.t.) ([ ] indicates 5,12- or 5,13- isomer): δ 9.76 (d, J

= 7.6 Hz, [5,13], 2H), 9.74 (d, J = 8.0 Hz, [5,12], 2H), 9.10 (s, [5,13], 2H), 9.05 (s, [5,12], 2H), 9.00 (d, J = 8.4 Hz, [5,12], 2H), 8.95 (d, J = 8.4 Hz, [5,13], 2H), 5.05 (t, J = 15.2 Hz, 4H). Anal. Calcd for $C_{34}H_{10}F_{14}N_4O_4$: C, 50.76; H, 1.25; N, 6.96, found: C, 50.88; H, 1.41; N, 7.17. Plate-shaped brown single crystals of **PDI−FCN₂** were grown by physical vapor transport technique under ambient atmosphere. The single crystal obtained was measured at 298 K. A total of 7133 reflections were measured at the maximum 2θ angle of 68.250°, of which 2609 were independent reflections (R_{int} = 0.0983). The analysis was carried out with space group of $P\bar{1}$ without disorder expediently. The crystal data are as follows: $C_{34}H_{10}F_{14}N_4O_4$; FW = 804.46, Triclinic, $P\bar{1}$, a = 5.2871(19) Å, b = 7.5621(19) Å, c = 19.404(5) Å, α = 90.49(2)°, β = 94.95(3)°, γ = 105.14(3)°, V = 745.7(4) Å^3, Z = 1, D_{calcd} = 1.791 g cm^{-3}, $F(000)$ = 400.0, μ = 1.602 (mm^{-1}), the refinement converged to R_1 [$I>2\sigma(I)$] = 0.1616, wR_2 (all data) = 0.4586, GOF = 1.222 (CCDC-1938639).

Section S2. Results of DFT calculations

Table S1. Intermolecular interaction energy (kcal/mol) of BQQDIs and PDIs based on the crystal structure with substitution of side chains with hydrogen.

	C_8–BQQDI	PhC_2–BQQDI	C_8–PDI	PDI–FCN_2
M06-2X/6-31++G**	−7.97	−7.36	−5.40	−3.37
MP2/6-31++G**	−8.62	−8.22	−5.78	−4.19

Table S2. Intermolecular interaction energy (kcal/mol) of BQQDIs and PDIs based on the crystal structure.

	C_8–BQQDI	PhC_2–BQQDI	C_8–PDI
M06-2X/6-31++G**	−7.79	−8.48	−5.16

Section S3. Details of instrumental characterizations

Table S3. Summary of cyclic voltammetry.

Compounds	$E_{0/-1}$ (V)	$E_{-1/-2}$ (V)	E_{LUMO} (V)
4-Hep−BQQDI	−0.69	−0.97	−4.11
4-Hep−PDI	−1.02	−1.26	−3.78 ($^{lit.}$−3.84(61))
PDI−FCN$_2$	−0.53	−0.86	−4.27

*$E_{0/-1}$ and $E_{-1/-2}$ attributes to the half-wave reduction potentials corresponding to the first- and second-redox reactions, respectively (vs. Fc/Fc$^+$). E_{LUMO} (vs. vacuum level) is estimated from $E_{0/-1}$: $E_{LUMO} = -4.8 - E_{0/-1}$.

Table S4. Summary of TG−DTA.

Compounds	T_{onset} (°C)	$T^{95\%}$ (°C)
PhC$_2$−BQQDI	354	421
C$_8$−BQQDI	303	377
PhC$_2$−PDI	370	429
C$_8$−PDI	306	402
PDI−FCN$_2$	279	342

$^†T_{onset}$: the onset temperature of weight loss; T_{95}: the temperature at which the weight fraction is 95%.
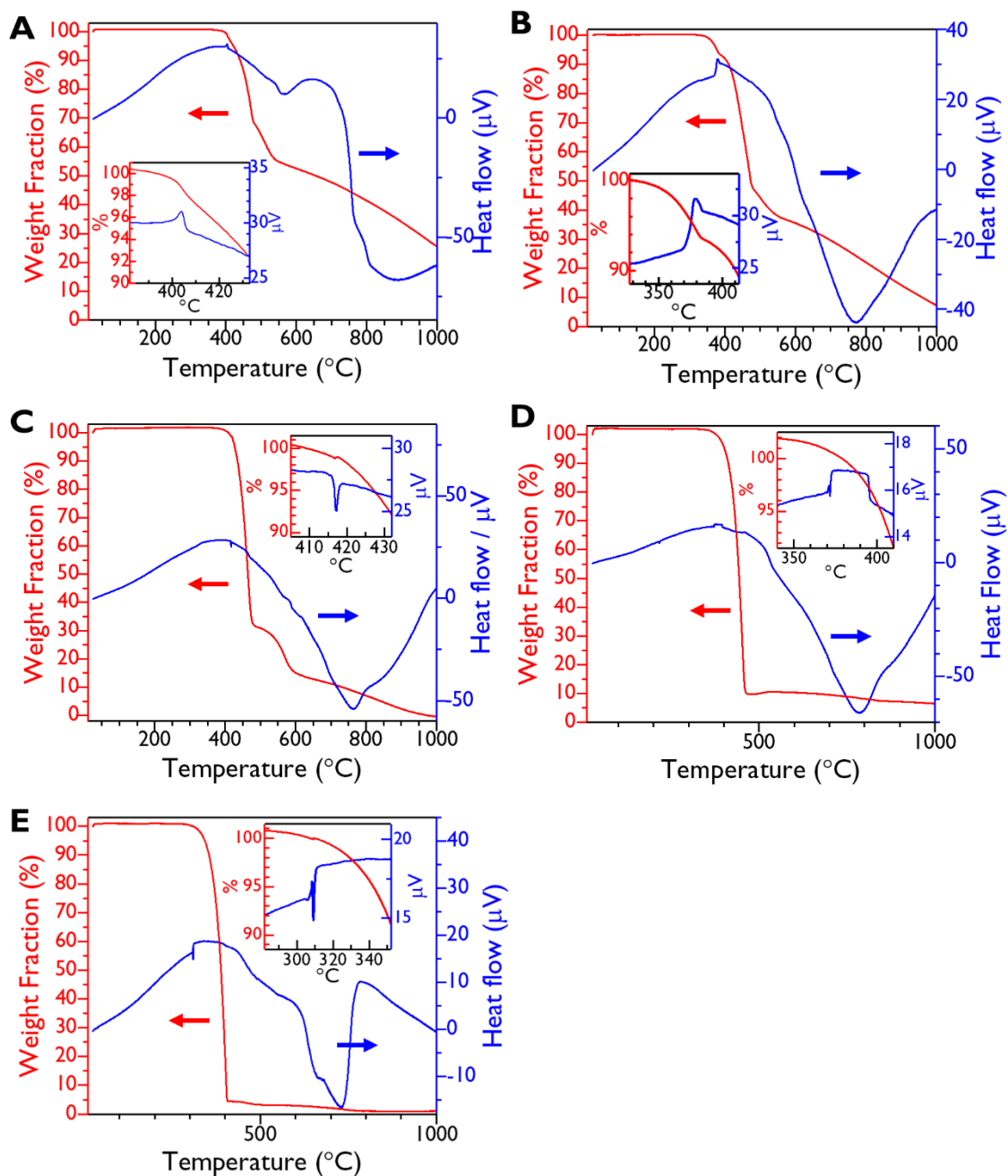
Fig. S18. TG−DTA profiles. Measurements were carried out under a nitrogen stream at the heating rate of 1 K min^{-1}. (**A**) **PhC$_2$−BQQDI**, (**B**) **C$_8$−BQQDI**, (**C**) **PhC$_2$−PDI**, (**D**) **C$_8$−PDI** and (**E**) **PDI−FCN$_2$.** Red and blue lines represent the residual weight fraction (left axis) and the heat flow (right axis), respectively. Insets: magnifications of the first inflection point of the weight fraction.

Photophysical properties

Intense optical absorptions in the UV-vis region are characteristic features of **BQQDI** and **PDI** derivatives. Fig. S2A displays a photograph of benzonitrile solutions (4×10^{-5} M) of **4-Hep−BQQDI** and **4-Hep−PDI**. While **4-Hep−PDI** results in an orange solution, **4-Hep−BQQDI** affords a yellow solution. The difference in the color can be explained by the UV-vis absorption spectra shown in Fig. S2B. **4-Hep−BQQDI** showed absorption peaks at 520, 485, 455 and 430 nm. On the other hand, **4-Hep−PDI** showed absorption peaks at 529, 492, 461 and 433 (shoulder) nm. Thus, **4-Hep−BQQDI** exhibits quite similar photophysical properties to those of **4-Hep−PDI**, except the red-shift features which is principally due to a reduced molecular symmetry in **BQQDI** structure compared with that of **PDI**. A slightly smaller absorbance in **4-Hep−BQQDI** is also attributable to the same origin. In addition, we compared optical absorption properties of **PhC₂−BQQDI** in a benzonitrile solution and in a vacuum-deposited solid film (Figs. S2C-D). Although the solubility was much poorer than that of **4-Hep−BQQDI**, **PhC₂−BQQDI** in a solution state exhibited an UV-vis absorption spectrum identical to **BQQDI** core. In the solid film, the absorption bands were broadened, and a new band appeared at red-shifted region, which was attributable to the aggregation in the solid state. As well, optical absorption spectra were measured and used for investigating materials stabilities of **PhC₂−BQQDI**, **C₈−BQQDI** and **PhC₂−PDI** under ambient atmosphere (Figs. S19C and S19E-G). Interestingly, **PhC₂−BQQDI** and **C₈−BQQDI** films showed remarkably different UV-vis absorption spectra, while they were composed of the same π-electron system. This might be due to different aggregated structures as likely seen in their single crystal structure determinations. UV-vis absorption spectrum of the vacuum-deposited **PhC₂−PDI** film is likely a mixture of the amorphous and crystalline phases(*62*). With time spent, the absorbance at 607 nm became increased while that at 492 nm decreased, which indicated that the amorphous phase partly turned into crystalline phase.
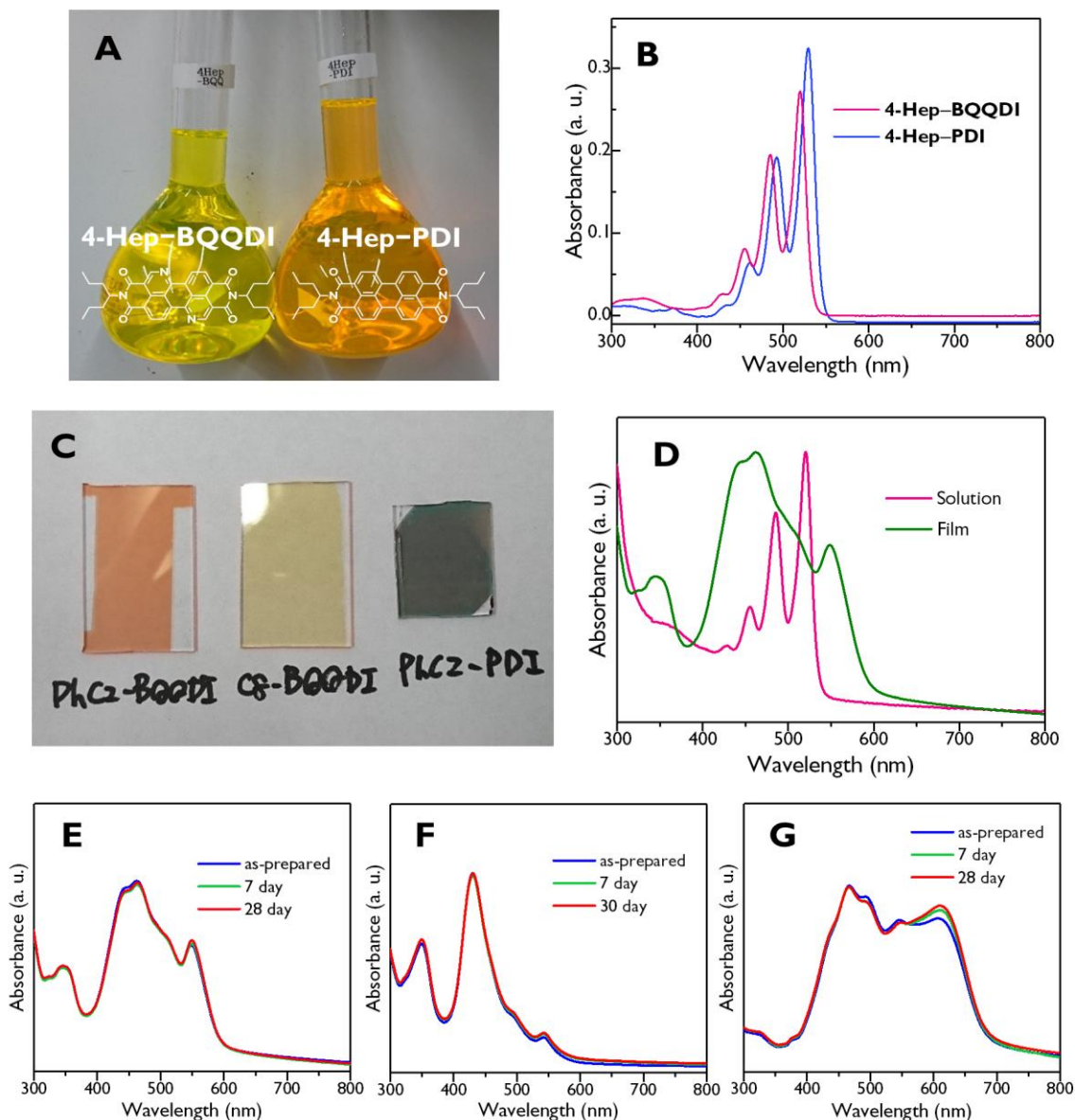
Fig. S19. Photophysical characterization. (**A**) Photograph of **4-Hep−BQQDI** (left) and **4-Hep−PDI** (right) solutions in benzonitrile (4×10^{-5} M). (**B**) UV-vis absorption spectra of **4-Hep−BQQDI** (blue) and **4-Hep−PDI** (magenta) in 4×10^{-6} M benzonitrile solutions. (**C**) Photograph of vacuum-deposited thin films (100 nm-thick) on quartz substrates under room light. Left: **PhC₂−BQQDI**, Center: **C₈−BQQDI**, Right: **PhC₂−PDI**. (**D**) Comparison of UV-vis absorption spectra of **PhC₂−BQQDI** in a benzonitrile solution (10^{-6} M; green) and in a vacuum-deposited thin film state (100 nm thick; pink). (**E-G**), Time-dependent UV-vis absorption spectra of vacuum-deposited 100 nm-thick films of **PhC₂−BQQDI**, **C₈−BQQDI** and **PhC₂−PDI**, respectively.

Section S4. Characterization of vacuum-deposited PC-TFTs

Device evaluations of vacuum-deposited PC-TFTs

    Analyses of the vacuum-deposited PC-TFTs in an argon-filled glovebox and in an air are summarized in Table S5 and Fig. S20.

Table S5. Summary of vacuum-deposited PC-TFT performances in an argon-filled glovebox and in an air.

Compounds	in glovebox			in air		
	Max. μ_e [cm^2 V^{-1} s^{-1}]	Avg. μ_e [cm^2 V^{-1} s^{-1}]	V_{th} [V]	Max. μ_e [cm^2 V^{-1} s^{-1}]	Avg. μ_e [cm^2 V^{-1} s^{-1}]	V_{th} [V]
PhC$_2$−BQQDI	0.55	0.49(2)	−0.6(6)	0.49	0.43(3)	1.7(4)
C$_8$−BQQDI	0.29	0.27(2)	4.2(1)	0.34	0.33(1)	5.3(3)
PhC$_2$−PDI	0.01	0.098(1)	5.3(2)	2.5×10^{-2}	0.021(1)	22.2(7)
C$_8$−PDI	0.44	0.41(4)	15.5(6)	0.50	0.28(15)	25(12)
PDI−FCN$_2$	0.38	0.33(7)	−4.0(5)	0.31	0.27(3)	−5.0(7)

[†]Data are extracted from 2−8 devices. Devices were thermally annealed at 100 °C for 2 h in a glovebox before measurement. $L = 200$ μm, $W = 1000$ μm. $V_D = 50$ V.
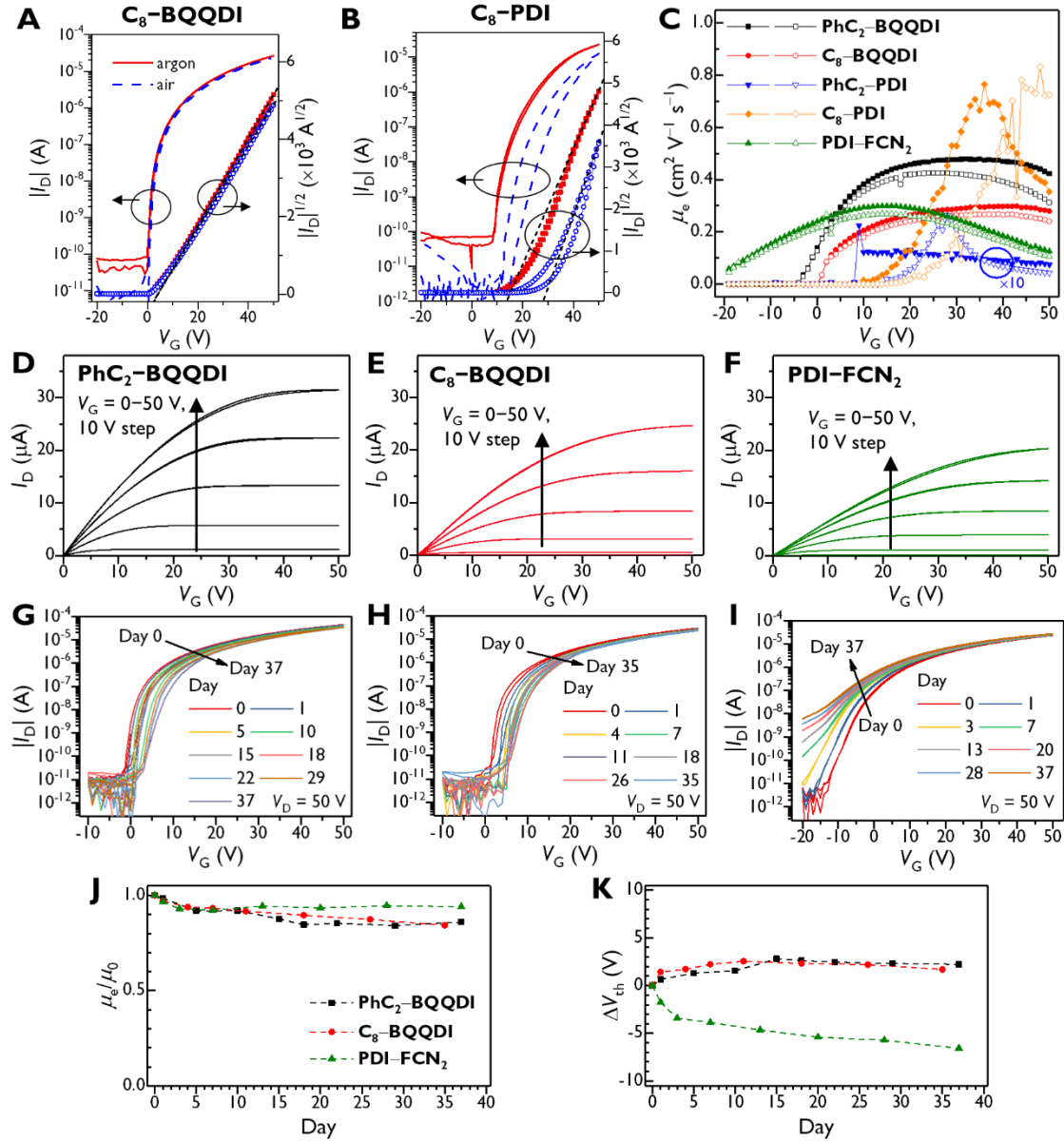
Fig. S20. Properties and durability of vacuum-deposited PC-TFTs in ambient air. TFT structures: **Sub** = **G** = n^{++}-Si; **Ins** = SiO$_2$ (200 nm) + DTS-SAM, C_i = 17.3 nF cm^{-2}; **S/D** = Au (60 nm). Transfer characteristics of (**A**) **C$_8$–BQQDI** and (**B**) **C$_8$–PDI** with V_D = 50 V, under Ar (red) and air (blue). Black dashed lines are the fits to $|I_D|^{1/2}$–V_G plots to estimate μ_e and V_{th}. (**C**) PC-TFT μ_e values as functions of V_g. The μ_e values determined from the plateaus in the plots for **PhC$_2$–BQQDI**, **C$_8$–BQQDI**, **PhC$_2$–PDI**, and **PDI–FCN$_2$** confirm the validity of the mobility assessment. In contrast, the peak-shaped plot for **C$_8$–PDI** indicates that μ_e was overestimated(*63*). (**D-F**) Output curves for **PhC$_2$–BQQDI**, **C$_8$–BQQDI**, and **PDI–FCN$_2$**, respectively, in air in the V_G range of 0–50 V with 10 V steps. (**G-I**) Changes in the transfer properties of TFTs incorporating **PhC$_2$–BQQDI**, **C$_8$–BQQDI**, and **PDI–FCN$_2$** during storage as determined under ambient conditions for approximately one month. While a gradual negative shift in V_{th} is observed for **PhC$_2$–BQQDI** and **C$_8$–BQQDI**, a significant positive change in V_{th}

accompanied by an increase in the off current is evident for **PDI–FCN₂**. (**J,K**) μ_e (normalized relative to the initial value, μ_0) and V_{th} shifts (ΔV_{th}) as functions of time, respectively.

Surface morphologies of the PC thin films were studied by AFM. Comparing **PhC₂−BQQDI** and **C₈−BQQDI**, fiber-like grains can be seen for the former, while plate-like grains are predominant for the latter. The morphology of **PhC₂−PDI** is similar to that of **PhC₂−BQQDI**, while the grain size seems smaller. **C8−PDI** formed relatively larger plate-like grains, suitable for charge-carrier transport. **PDI−FCN₂** formed plate-like grains as seen in **C₈−BQQDI**, while the grains are small.
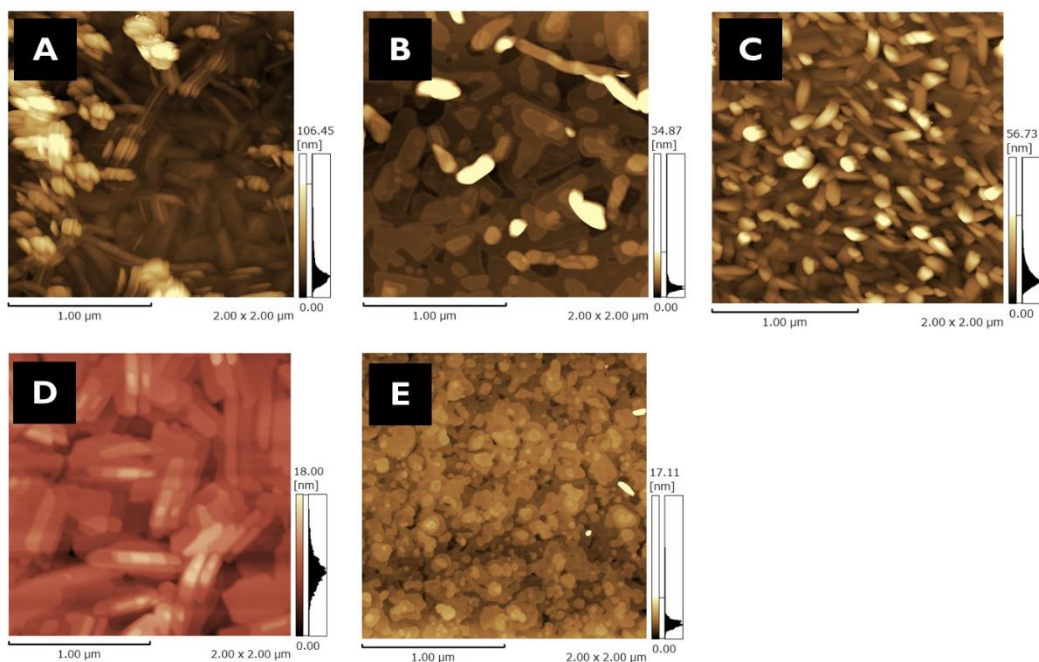
Fig. S21. AFM images of vacuum-deposited thin films. 40 nm-thick films were deposited on DTS-SAM modified SiO₂. (**A**) **PhC₂−BQQDI**, (**B**) **C₈−BQQDI**, (**C**) **PhC₂−PDI**, (**D**) **C₈−PDI** and (**E**) **PDI−FCN₂**.

<u>Thin-film X-ray diffraction on vacuum-deposited PC thin films</u>

Thin-film out-of-plane X-ray diffraction profiles are shown in Fig. S22. **PhC$_2$−BQQDI** showed diffraction peaks at 2θ of 4.00° (d = 22.0 Å), 4.82° (18.3 Å) and 15.92 (5.6 Å), 19.81 (4.5 Å) and 24.9° (3.6 Å), suggesting that PC film of **PhC$_2$−BQQDI** is composed of mixture, one of which is consistent with the single crystal structural data. For **C$_8$−BQQDI**, the diffractions were observed at 2θ of 3.31° (26.7 Å), 10.02° (8.8 Å), 13.28° (6.6 Å), 16.58 (5.3 Å) and 23.32° (3.8 Å), being consistent with the single crystal structural data. **PhC$_2$−PDI** showed the diffractions at 2θ = 5.75° (15.3 Å), being consistent with the literature(*64*). For **C$_8$−PDI**, the observed diffractions were at 2θ of 4.34° (20.3 Å), 8.69° (10.2 Å), 13.00° (6.8 Å), 17.32° (5.1 Å), 21.75° (4.1 Å) and 26.13° (3.4 Å), indicating a high degree of layer-by-layer structural order and being consistent with the literature(*65*). As for **PDI−FCN$_2$**, the diffraction peaks were observed at 8.81° (10.0 Å) and 13.32° (6.6 Å), where the latter was consistent with the literature while the former had not been visible.
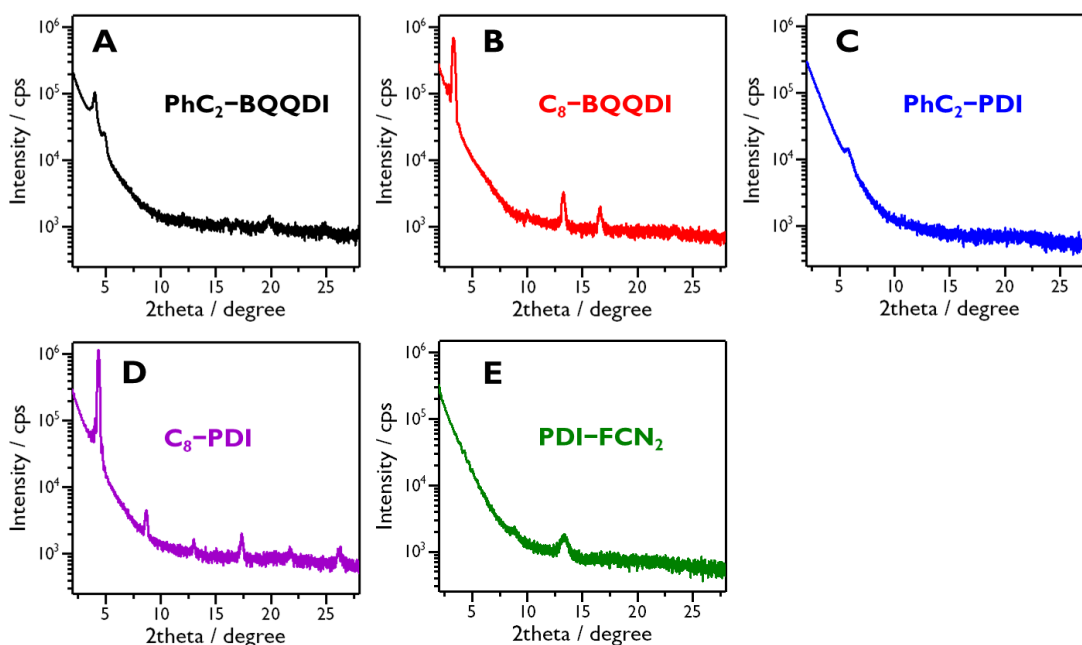
Fig. S22. Out-of-plane X-ray diffraction profiles of vacuum-deposited thin films. (A) **PhC$_2$−BQQDI**, (B) **C$_8$−BQQDI**, (C) **PhC$_2$−PDI**, (D) **C$_8$−PDI** and (E) **PDI−FCN$_2$** vacuum-deposited 40 nm-thick PC films on DTS-SAM modified SiO$_2$ at 140 °C.

Section S5. Characterization of solution-deposited SC-TFTs
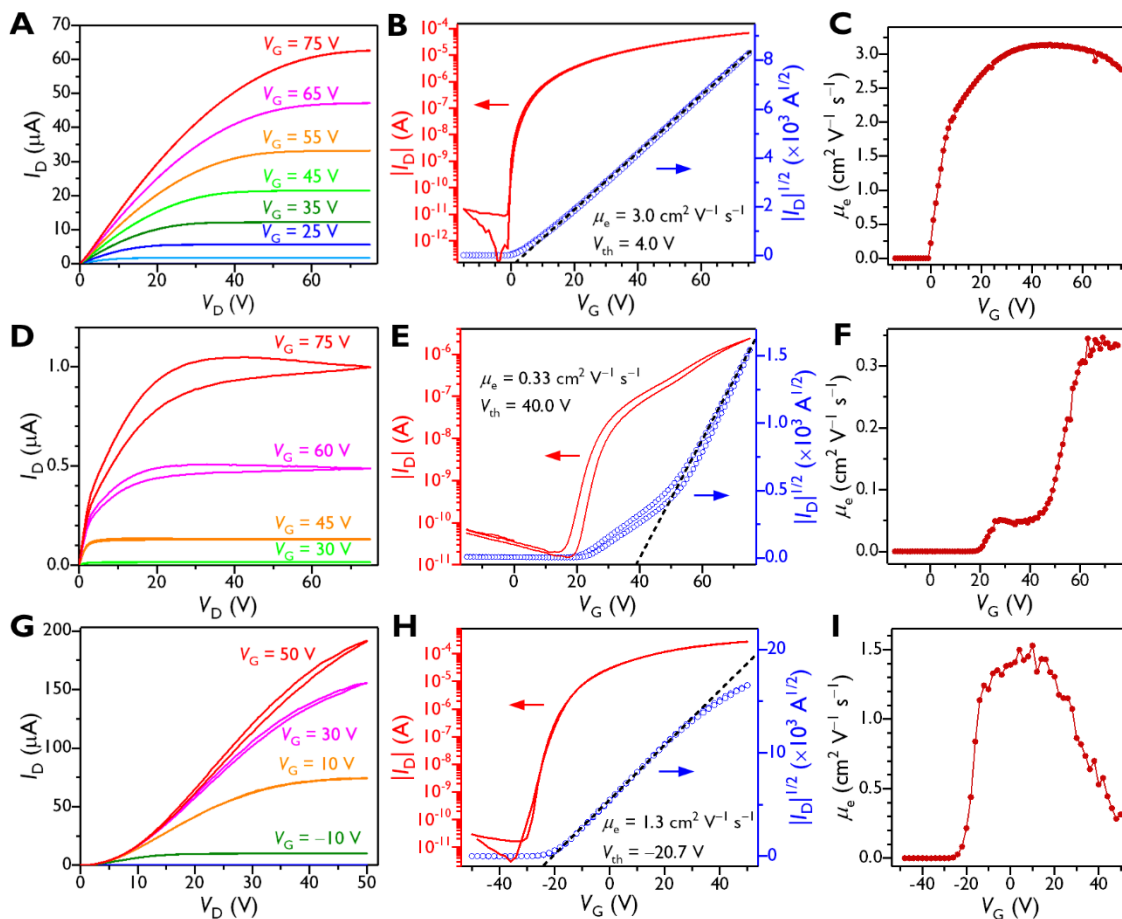
Fig. S23. SC-TFT characterizations under ambient conditions. TFT structures: **Sub** = **G** = n^{++}-Si, **Ins** = SiO$_2$ (200 nm) + AL-X601 (25–60 nm), C_i = 12.5–15 nF cm^{-2}; **S/D** = Au (40 nm). Output curves, transfer characteristics, and effects of V_G on μ_e for (**A-C**) **PhC2–BQQDI**, (**D-F**) **C8–BQQDI**, and (**G-I**) **PDI–FCN2**, respectively, having L/W (μm/μm) ratios of 190/136 (1.4), 91/75 (1.2) and 94/660 (0.14). Transfer characteristics determined at V_D values of 75, 75, and 50 V, respectively. The black dashed lines in the transfer characteristic plots are fits to $|I_D|^{1/2}$–V_G used to estimate μ_e and V_{th}.
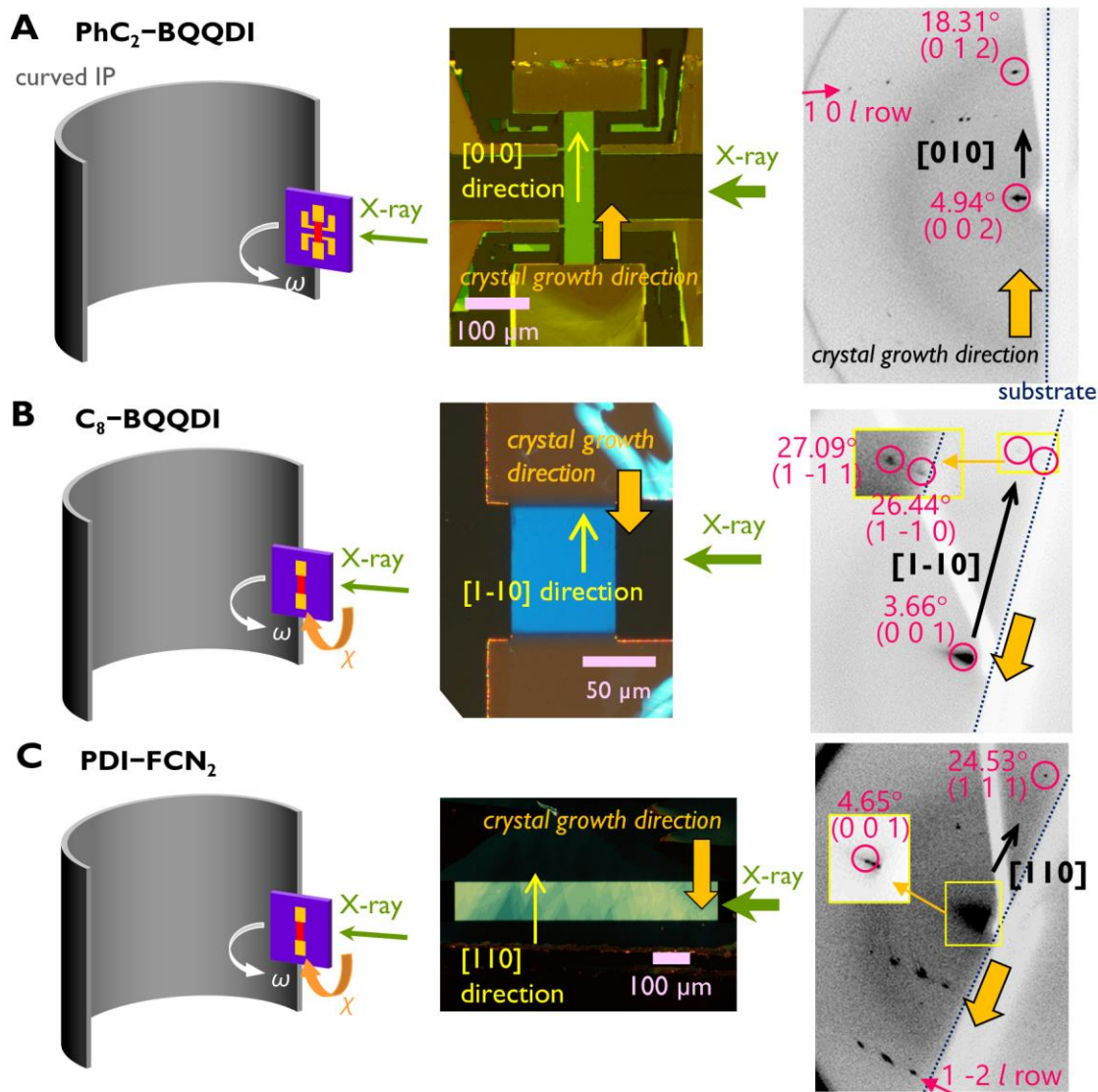
Fig. S24. Determination of the direction of the crystallographic axis. (**A**) **PhC₂–BQQDI**, (**B**) **C₈–BQQDI**, and (**C**) **PDI–FCN₂**. For each row, the left panel schematically illustrates the experimental setup (with "IP" indicating the imaging plate), the central panel shows a polarized optical microscopy image of the SC film (with the crystallographic axis indicated), and the right panel shows the X-ray oscillation image acquired along the out-of-plane direction (*i.e.*, the X-ray was almost parallel to the substrate) at room temperature. The oscillation images were obtained in the ω-scan mode with $\varphi = 0°$ and $\chi = 0°$ for **PhC₂–BQQDI**, $\chi = 20°$ for **C₈–BQQDI**, and $\chi = 25°$ for **PDI–FCN₂**. From these analyses, the crystallographic axes along the channel of each TFT, which also correspond to the direction of thin-film crystal growth, were determined to be approximately [010], [1-10], and [110] for the **PhC₂–BQQDI**, **C₈–BQQDI**, and **PDI–FCN₂**, respectively.

<u>PhC$_2$−BQQDI</u> <u>with</u> <u>β−PTS-SAM/SiO$_2$ dielectric</u> <u>layer:</u> <u>sample-to-sample variation</u>

   Although the AL-X601 polymer insulator surface has exhibited well wettability and electron mobility up to 3.0 cm^2 V^{-1} s^{-1} for **PhC$_2$−BQQDI** SC-TFT, sample-to-sample mobility variation likely due to the quality of formed AL-X601 layer has been observed. On the other hand, **PhC$_2$−BQQDI** SC-TFTs can also be fabricated using silicon wafer substrates with β−PTS-SAM modified SiO$_2$ layer, where the variation of surface condition should be suppressed compared with polymer insulator. Therefore, the device anisotropy and sample-to-sample variation of the **PhC$_2$−BQQDI** SC-TFT were evaluated using the β−PTS-SAM functionalized SiO$_2$ dielectric surface. Representative output and transfer (V_D = 50 V) characteristics are shown in Fig. S25A and 25B, respectively, with μ_e = 2.23 cm^2 V^{-1} s^{-1}. 15 SC-TFTs studied herein revealed high carrier mobilities of μ_e = 2.2±0.3 cm^2 V^{-1} s^{-1} (the maximum μ_e = 2.57 cm^2 V^{-1} s^{-1}) and V_{th} =4.3±1.6 V. The intrinsic nature of small sample-to-sample variation and high μ_e is verified in the superimposed V_G-dependent μ_e curves (Fig. S25C). In Fig. S25B, the fit to $|I_D|^{1/2}$ (black broken line) and the slope of an electrically equivalent ideal TFT (magenta solid line) are shown, estimating the reliability factor (r)(*41*) of 87% in this device. The r for all 15 TFTs are summarized in Fig. S25D, where the r is ranging from 81% to 91%. Hence, the effective mobility (μ_{eff}), which is estimated by $\mu_e \times r$, has a distribution between 1.64 and 2.16 cm^2 V^{-1} s^{-1} as shown in Fig. S25E.
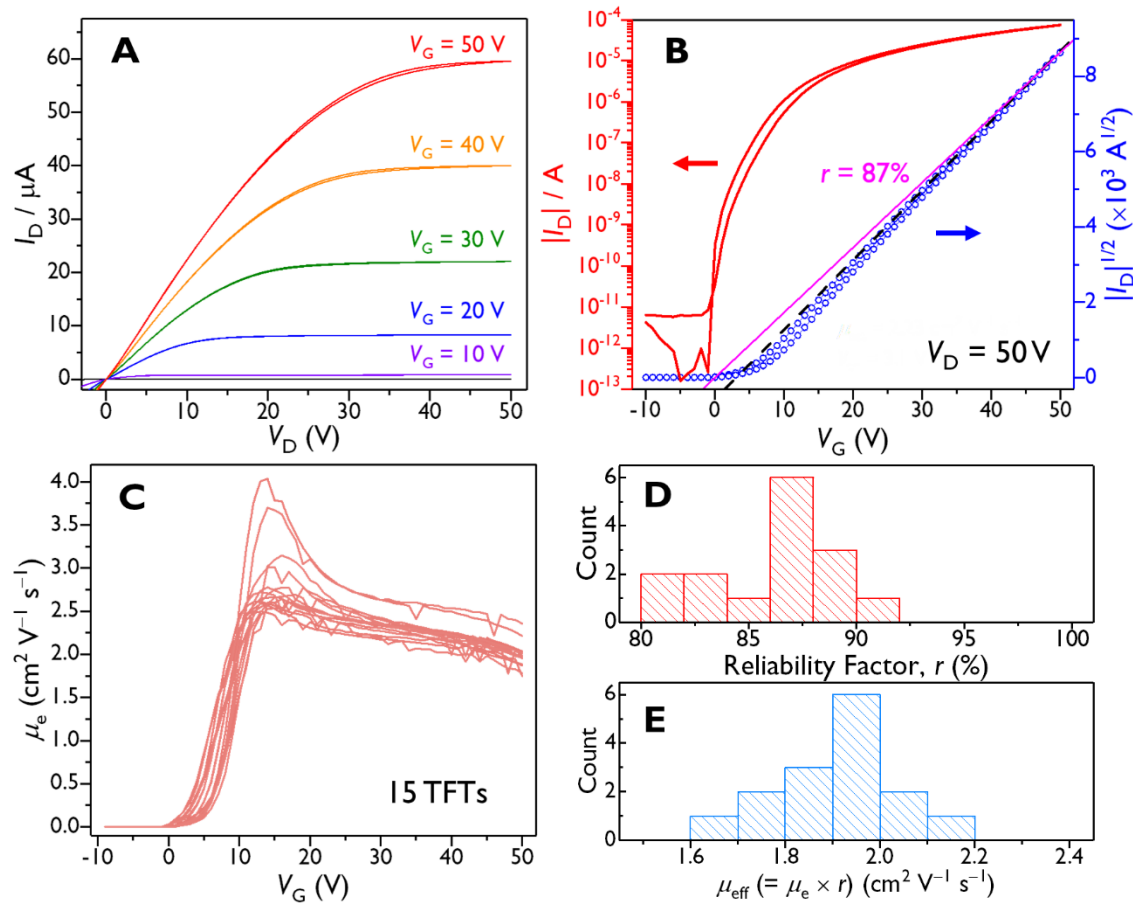
Fig. S25. SC-TFT performances of PhC$_2$−BQQDI on a β−PTS-SAM modified silicon wafer.
TFT structure: **G** = n^{++}-Si, **Ins** = SiO$_2$ (200 nm) + β−PTS-SAM; C_i = 17.3 nF cm^{-2}, **OSC** =

PhC$_2$−BQQDI, **S/D** = Au (40 nm). Representative (**A**) output and (**B**) transfer (V_D = 50 V) curves under ambient condition. Black broken line is the fit to $|I_D|^{1/2}$−V_G plot. Magenta solid line represents the slope of an electrically equivalent ideal TFT(*41*), indicating the reliability factor (*r*) of 87%. (**C**) μ_e plotted as a function of V_G of 15 SC-TFTs. (**D-E**) Statics of *r* and the effective mobility (μ_{eff}; μ_{eff} = $\mu_e \times r$) corresponding to the 15 SC-TFTs.

Section S6. Gated Hall effect measurement on PhC₂−BQQDI

The SC-TFT device of **PhC₂−BQQDI** used for gated Hall effect measurements was fabricated in the same manner as the SC-TFT units described above, except for the use of a metal shadow mask having a Hall bar geometry. An n^{++}-doped silicon wafer with a 200 nm-thick SiO₂ layer and coated with AL-X601 (~31 nm) was used as the substrate. The laser etching allowed the formation of a well-defined Hall bar architecture with $L/W = 235/48$ and a longitudinal interprobe (V₁−V₂ and V₃−V₄ shown in Fig. S26A) distance (D) of 115 μm. The gated Hall effect measurements were performed using a helium gas-exchanged cryostat with a superconducting magnet at 300 K. While the magnetic field (B) was swept between 12 and −12 T, transistor operation was conducted using a Keithley 2634B source meter with $V_D = 1.5$ V. Longitudinal (V_{long}) and transverse (V_{trans}) electromotive forces were monitored with Agilent 34410A 6½ digit multimeters.

Sheet conductivity (σ_{sh}) at each V_G was calculated by $I_D D/V_{long}W$, shown in Fig. S26B. As a result, the four-terminal field-effect mobility (μ_{4T}) was estimated to be 4.1 cm² V^{-1} s^{-1} with $V_{th} = 13.0$ V.

Hall coefficient (R_{Hall}) was estimated from V_{trans} by using the following equation:

$$V_{trans} - V_{B=0} = R_{Hall}I_D B,$$

where $V_{B=0}$ stands for the V_{trans} when $B = 0$ T. $(R_{Hall})^{-1}$ was plotted as a function of V_G (Fig. S26C), in which the negative sign of R_{Hall} was consistent with the n-type TFT operation. In addition, the Hall carrier density (n_{Hall}) was estimated from the following relationship:

$$n_{Hall} = \frac{1}{qR_{Hall}},$$

where q is the elementary charge. $(R_{Hall})^{-1}$ dependent on V_G was thus transformed into V_G-dependent n_{Hall}, as shown in Fig. S26D. Simultaneously, the sheet carrier density accumulated by field effect (n_{FE}), which was calculated from C_i ($n_{FE} = C_i|V_G - V_{th}|/q$), was also plotted as a function of $|V_G - V_{th}|$ (blue solid line). Here, the slopes of calculated n_{FE} and the linear fit to n_{Hall} are directly compared due to the ideal relationship $n = (qR_{Hall})^{-1}$, confirming a well-consistent feature with the so-called coherence factor determined by n_{FE}/n_{Hall} of 1.0. The coherence factor of 1 means the entire field-accumulated charge carriers are coherently mobile, which indicates an ideal band-like electron transport at the semiconductor−dielectric interface. The Hall mobility (μ_{Hall}) estimated by $R_{Hall}\cdot\sigma_{sh}$ was 4.0 cm² V^{-1} s^{-1}, being consistent with the μ_{4T} and the coherence factor of 1.
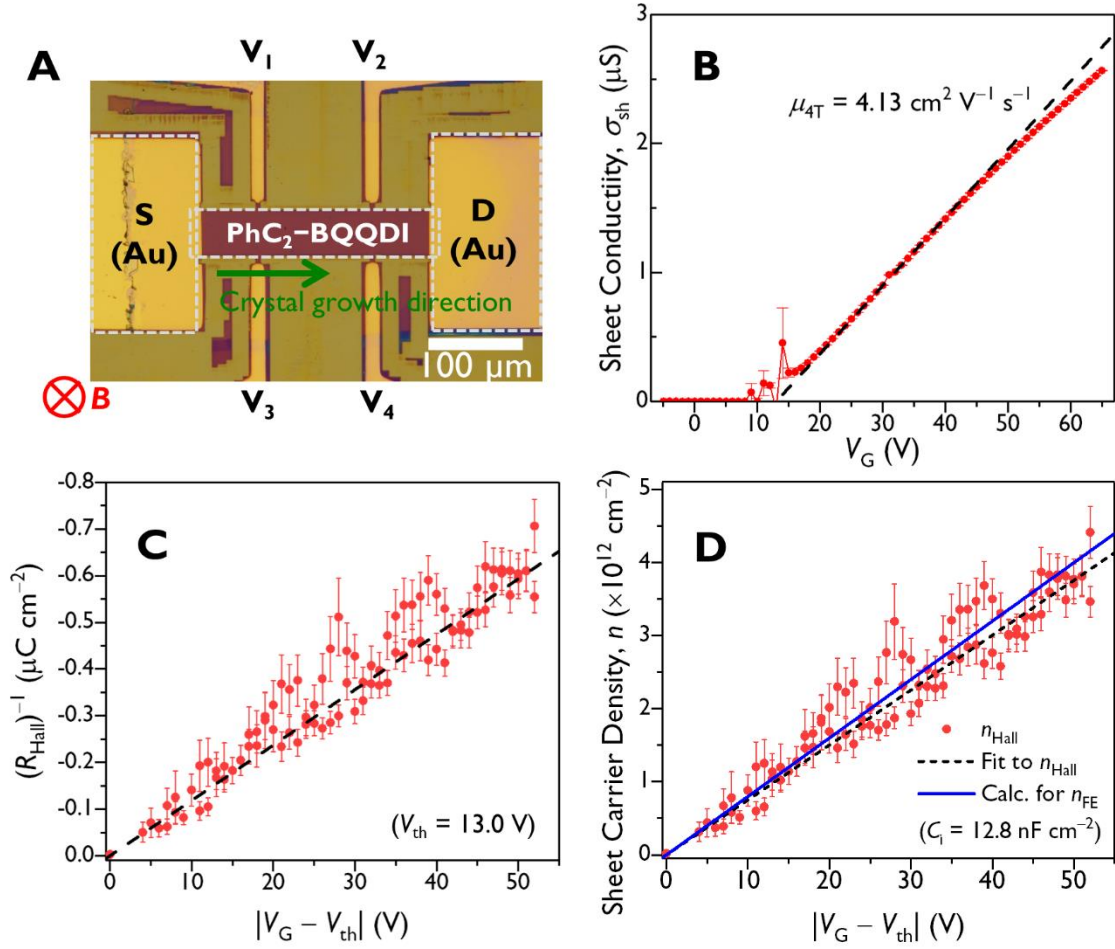
Fig. S26. Gated Hall effect measurement on PhC₂−BQQDI SC-TFT. TFT structure: **Sub** = **G** = n^{++}-Si, **Ins** = SiO$_2$ (200 nm) + AL-X601 (31 nm), C_i = 12.8 nF cm^{-2}; **S/D** = Au (40 nm). (**A**) Optical microscope image of the channel region. (**B**) V_G-dependent σ_{sh} estimated by the 4-terminal geometry. Black dashed line is the linear fit, affording the μ_{4T} of 4.13 cm^2 V^{-1} s^{-1}. (**C**) $(R_{Hall})^{-1}$ as a function of $|V_G − V_{th}|$ at 300 K (V_{th} = 13.0 V). Black dashed line is the linear fit. (**D**) Sheet carrier densities as a function of $|V_G − V_{th}|$. Black broken line is the linear fit to n_{Hall}. Blue solid line represents the theoretical sheet carrier density accumulated by the field effect (n_{FE}), calculated as $n_{FE} = C_i(V_G − V_{th})/q$.

Section S7. Thermal stress tests on PhC$_2$−BQQDI SC-TFTs on different substrates
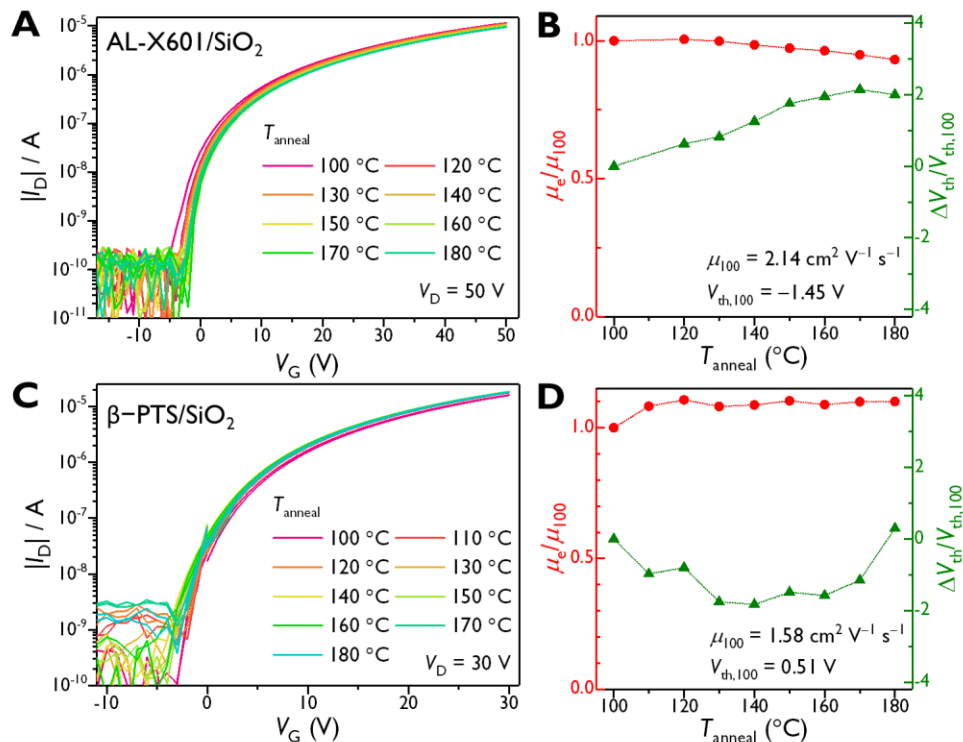
Fig. S27. Thermal stress test data for PhC$_2$–BQQDI SC-TFTs using different substrates. (**A, C**) and (**B, D**) provide the transfer curves obtained at various T_{anneal} values and the extracted μ_e/μ_{100} and $\Delta V_{th}/V_{th,100}$ values, respectively, with different substrates. TFT structures for **A-B**: **Sub** = **G** = n^{++}-Si, **Ins** = SiO$_2$ (200 nm) + AL-X601 (45 nm), C_i = 13.0 nF cm^{-2}; **S/D** = Au (40 nm). TFT structures for **C-D**: **Sub** = **G** = n^{++}-Si, **Ins** = SiO$_2$ (100 nm) + β–PTS-SAM, C_i = 34.5 nF cm^{-2}; **S/D** = Au (40 nm).

Section S8. Details of MD simulation and estimated dynamic fluctuations

Table S6. Number of molecules, temperature, and MD cell size and shape.

	PhC$_2$−BQQDI	**C$_8$−BQQDI**	**PDI−FCN$_2$**	**PhC$_2$−PDI**
Num. of molecules	672	560	576	672
Temperature (K)	296	300	298	298
Crystal syst.	monoclinic	triclinic	triclinic	monoclinic
Space group	$P2_1/n$	$P\bar{1}$	$P\bar{1}$	$P2_1/c$
a (nm)	7.705	4.710	5.287	4.737
b (nm)	5.022	6.671	7.562	32.450
c (nm)	35.810	26.091	19.404	9.507
α (°)	90.00	87.69	90.49	90.00
β (°)	92.47	89.71	94.95	100.27
γ (°)	90.00	74.79	105.14	90.00
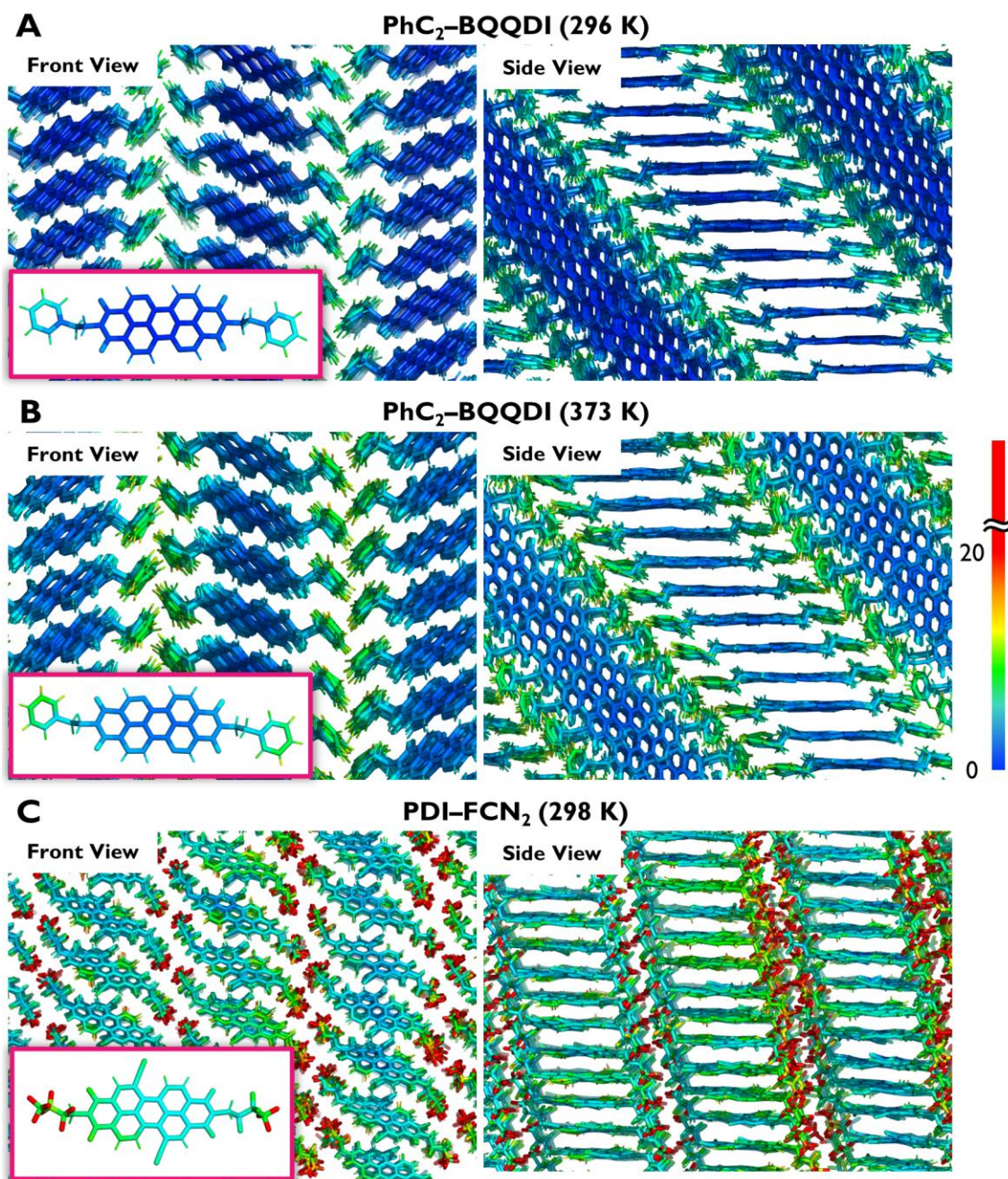
Fig. S28. Colour-coded *B*-factor distributions (unit: $\text{Å}^2\,\text{s}^{-1}$) obtained from the trajectories during the last 20 ns of 100 ns MD runs. (**A-B**) **PhC₂–BQQDI** (at 296 and 373 K, respectively). and (**C**) **PDI–FCN₂** (at 298 K). The initial structures for both were constructed from single-crystal structures obtained experimentally.
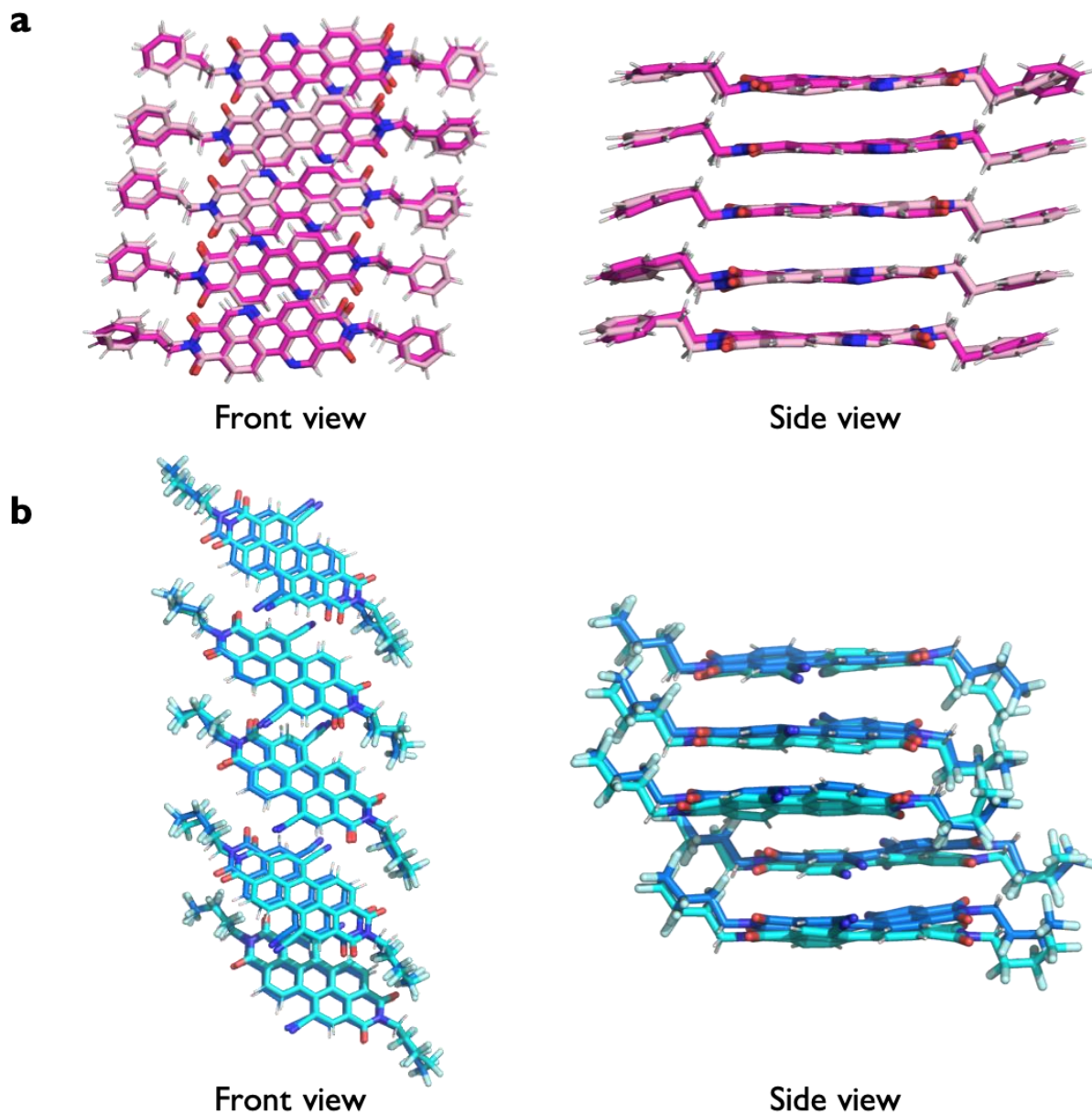
Fig. S29. Superimposed snapshots of the representative molecules after 100 ns and 100.1 ns of MD simulations. (**A**) Top and side views for **PhC$_2$−BQQDI** are shown as sticks colored by pale pink for 100 ns and magenta for 100.1 ns. (**B**) Top and side views for **PDI−FCN$_2$** are shown as cyan sticks for 100 ns and as azure sticks for 100.1 ns.

Dynamical fluctuation of transfer integrals

By using the atomic coordinates at the 100 ns acquired by the MD simulation, transfer integrals t_{1-3} corresponding to Figs. 3E-F in the main text were calculated over 141−209 dimers.
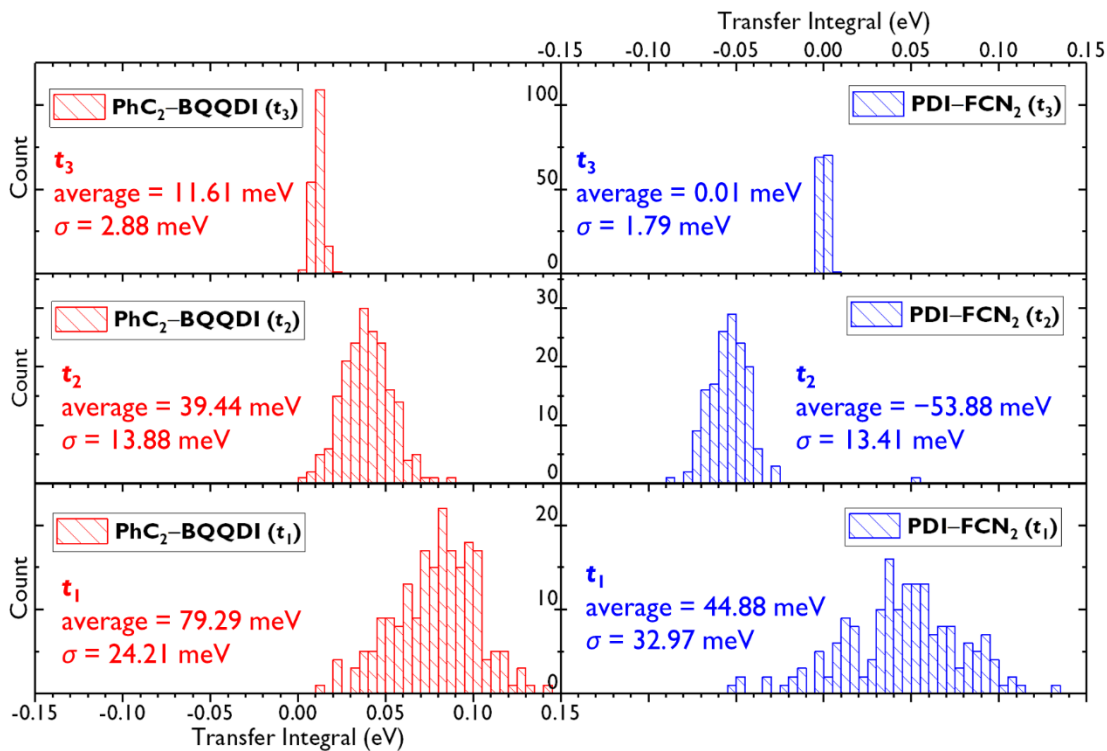
Fig. S30. Simulated dynamical fluctuation of transfer integral. Transfer integrals t_{1-3}, corresponding to Figs. 3E-F, of **PhC₂−BQQDI** and **PDI−FCN₂** at room temperature based on the atomic coordinates acquired by single crystal structure-based MD simulation.

Section S9. Evaluation of CMOS device

We evaluated a single CMOS inverter performance, confirming the full rail-to-rail swing (Fig. S31C), the voltage gain over 100 (Fig. S31C), and the standby power on the order of nano-watt (Fig. S31D).
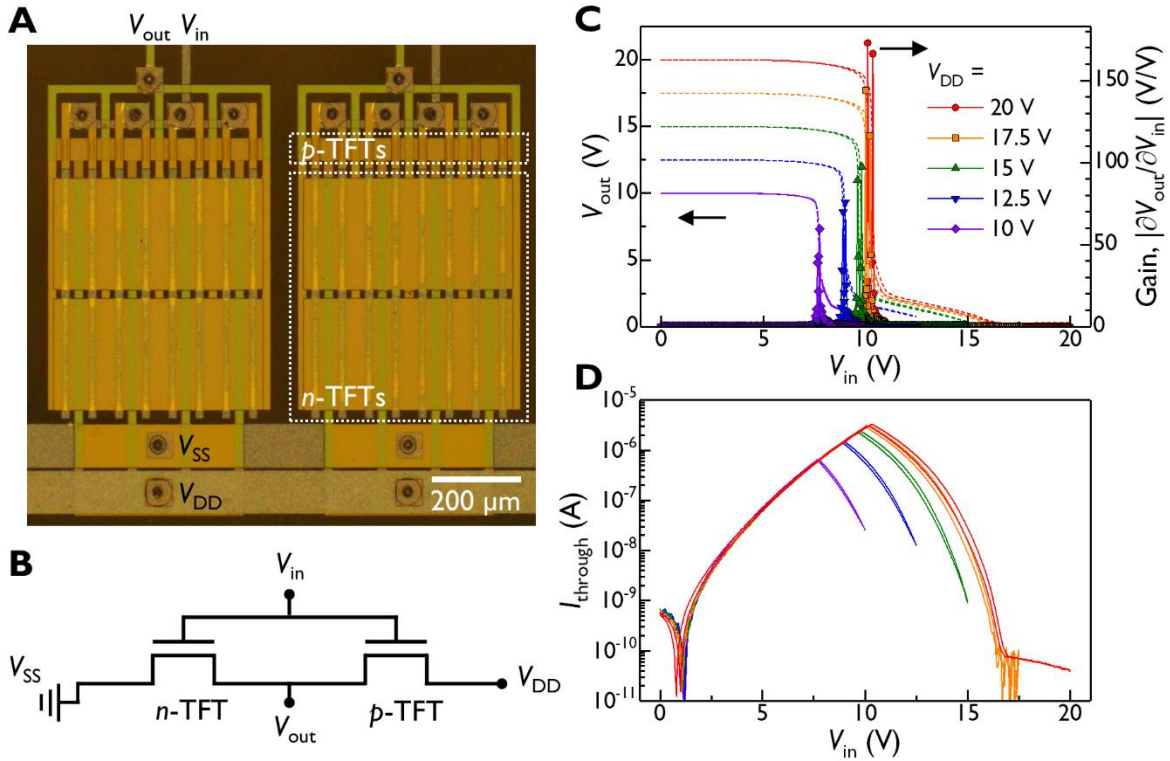
Fig. S31. CMOS inverters. (**A**) Polarized optical microscopy image of the photolithographically fabricated CMOS inverters. (**B**) Schematic circuit diagram of a single CMOS inverter. (**C**) Voltage transfer curves (corresponding to those shown in Fig. 6G) and corresponding voltage gains. (**D**) Through current ($I_{through}$) during the inverter operation.

Captions for Movie S1 to S4:

Movie S1. MD simulation of PhC$_2$−BQQDI at 296 K viewed from the side of the brickwork assembly during 80−100 ns run. Representative seven molecules are displayed, and the phenethyl moieties are omitted for clarity.

Movie S2. MD simulation of PhC$_2$−BQQDI at 296 K viewed from the front of the brickwork assembly during 80−100 ns run. Representative seven molecules are displayed, and the phenethyl moieties are omitted for clarity.

Movie S3. MD simulation of PDI−FCN$_2$ at 298 K viewed from the side of the brickwork assembly during 80−100 ns run. Representative seven molecules are displayed, and the 1H,1H-heptafluorobutyl moieties are omitted for clarity.

Movie S4. MD simulation of PDI−FCN$_2$ at 298 K viewed from the front of the brickwork assembly during 80−100 ns run. Representative seven molecules are displayed, and the 1H,1H-heptafluorobutyl moieties are omitted for clarity.

REFERENCES AND NOTES

1. Z. Bao, J. Locklin, *Organic Field-Effect Transistors* (CRC Press, ed. 1, 2007).

2. A. C. Arias, J. D. MacKenzie, I. McCulloch, J. Rivnay, A. Salleo, Materials and applications for large area electronics: Solution-based approaches. *Chem. Rev.* **110**, 3–24 (2010).

3. S.-S. Sun, N. S. Sariciftci, *Organic Photovoltaics: Mechanism, Materials, and Devices* (CRC Press, 2005).

4. K. Müllen, U. Scherf, *Organic Light-Emitting Devices: Synthesis, Properties and Applications* (Wiley-VCH, 2006).

5. J. L. Brédas, J. P. Calbert, D. A. da Silva Filho, J. Cornil, Organic semiconductors: A theoretical characterization of the basic parameters governing charge transport. *Proc. Natl. Acad. Sci. U.S.A.* **99**, 5804–5809 (2002).

6. E. F. Valeev, V. Coropceanu, D. A. da Silva Filho, S. Salman, J.-L. Brédas, Effect of electronic polarization on charge-transport parameters in molecular organic semiconductors. *J. Am. Chem. Soc.* **128**, 9882–9886 (2006).

7. V. Coropceanu, J. Cornil, D. A. da Silva Filho, Y. Olivier, R. Silbey, J.-L. Brédas, Charge transport in organic semiconductors. *Chem. Rev.* **107**, 926–952 (2007).

8. S. Illig, A. S. Eggeman, A. Troisi, L. Jiang, C. Warwick, M. Nikolka, G. Schweicher, S. G. Yeates, Y. Henri Geerts, J. E. Anthony, H. Sirringhaus, Reducing dynamic disorder in small-molecule organic semiconductors by suppressing large-amplitude thermal motions. *Nat. Commun.* **7**, 10736 (2016).

9. A. Troisi, G. Orlandi, J. E. Anthony, Electronic interactions and thermal disorder in molecular crystals containing cofacial pentacene units. *Chem. Mater.* **17**, 5024–5031 (2005).

10. A. Troisi, G. Orlandi, Charge-transport regime of crystalline organic semiconductors: Diffusion limited by thermal off-diagonal electronic disorder. *Phys. Rev. Lett.* **96**, 086601 (2006).

11. S. Ciuchi, S. Fratini, D. Mayou, Transient localization in crystalline organic semiconductors. *Phys. Rev. B* **83**, 081202 (2011).

12. A. S. Eggeman, S. Illig, A. Troisi, H. Sirringhaus, P. A. Midgley, Measurement of molecular motion in organic semiconductors by thermal diffuse electron scattering. *Nat. Mater.* **12**, 1045–1049 (2013).

13. T. Kubo, R. Häusermann, J. Tsurumi, J. Soeda, Y. Okada, Y. Yamashita, N. Akamatsu, A. Shishido, C. Mitsui, T. Okamoto, S. Yanagisawa, H. Matsui, J. Takeya, Suppressing molecular vibrations in organic semiconductors by inducing strain. *Nat. Commun.* **7**, 11156 (2016).

14. H. Ishii, J. Inoue, N. Kobayashi, K. Hirose, Quantitative mobility evaluation of organic semiconductors using quantum dynamics based on density functional theory. *Phys. Rev. B* **98**, 235422 (2018).

15. T. Okamoto, C. Mitsui, M. Yamagishi, K. Nakahara, J. Soeda, Y. Hirose, K. Miwa, H. Sato, A. Yamano, T. Matsushita, T. Uemura, J. Takeya, V-shaped organic semiconductors with solution processability, high mobility, and high thermal durability. *Adv. Mater.* **25**, 6392–6397 (2013).

16. C. Mitsui, T. Okamoto, M. Yamagishi, J. Tsurumi, K. Yoshimoto, K. Nakahara, J. Soeda, Y. Hirose, H. Sato, A. Yamano, T. Uemura, J. Takeya, High-performance solution-processable N-shaped organic semiconducting materials with stabilized crystal phase. *Adv. Mater.* **26**, 4546–4551 (2014).

17. K. Nakahara, C. Mitsui, T. Okamoto, M. Yamagishi, H. Matsui, T. Ueno, Y. Tanaka, M. Yano, T. Matsushita, J. Soeda, Y. Hirose, H. Sato, A. Yamano, J. Takeya, Furan fused V-shaped organic semiconducting materials with high emission and high mobility. *Chem. Commun.* **50**, 5342–5344 (2014).

18. C. Mitsui, H. Tsuyama, R. Shikata, Y. Murata, H. Kuniyasu, M. Yamagishi, H. Ishii, A. Yamamoto, Y. Hirose, M. Yano, T. Takehara, T. Suzuki, H. Sato, A. Yamano, E. Fukuzaki, T. Watanabe, Y. Usami, J. Takeya, T. Okamoto, High performance solution-crystallized thin-film transistors based on V-shaped thieno[3,2-*f*,4,5-*f'*]bis[1]benzothiophene semiconductors. *J. Mater. Chem. C* **5**, 1903–1909 (2017).

19. C. Mitsui, M. Yamagishi, R. Shikata, H. Ishii, T. Matsushita, K. Nakahara, M. Yano, H. Sato, A. Yamano, J. Takeya, T. Okamoto, Oxygen- and sulfur-bridged bianthracene V-shaped organic semiconductors. *Bull. Chem. Soc. Jpn.* **90**, 931–938 (2017).

20. A. Yamamoto, Y. Murata, C. Mitsui, H. Ishii, M. Yamagishi, M. Yano, H. Sato, A. Yamano, J. Takeya, T. Okamoto, Zigzag-elongated fused π-electronic core: A molecular design strategy to maximize charge-carrier mobility. *Adv. Sci.* **5**, 1700317 (2018).

21. T. Okamoto, Next-generation organic semiconductors driven by bent-shaped π-electron cores. *Polym. J.* **51**, 825–833 (2019).

22. H. Iino, T. Usui, J. Hanna, Liquid crystals for organic thin-film transistors. *Nat. Commun.* **6**, 6828 (2015).

23. J.-H. Dou, Y.-Q. Zheng, Z.-F. Yao, T. Lei, X. Shen, X.-Y. Luo, Z.-A. Yu, S.-D. Zhang, G. Han, Z. Wang, Y. Yi, J.-Y. Wang, J. Pei, A cofacially stacked electron-deficient small molecule with a high electron mobility of over 10 cm^2 V^{-1} s^{-1} in air. *Adv. Mater.* **27**, 8051–8055 (2015).

24. X. Xu, Y. Yao, B. Shan, X. Gu, D. Liu, J. Liu, J. Xu, N. Zhao, W. Hu, Q. Miao, Electron mobility exceeding 10 cm^2 V^{-1} s^{-1} and band-like charge transport in solution-processed n-Channel organic thin-film transistors. *Adv. Mater.* **28**, 5276–5283 (2016).

25. H. Usta, A. Facchetti, T. J. Marks, n-Channel semiconductor materials design for organic complementary circuits. *Acc. Chem. Res.* **44**, 501–510 (2011).

26. X. Zhan, A. Facchetti, S. Barlow, T. J. Marks, M. A. Ratner, M. R. Wasielewski, S. R. Marder, Rylene and related diimides for organic electronics. *Adv. Mater.* **23**, 268–284 (2011).

27. A. S. Molinari, H. Alves, Z. Chen, A. Facchetti, A. F. Morpurgo, High electron mobility in vacuum and ambient for PDIF-CN$_2$ single-crystal transistors. *J. Am. Chem. Soc.* **131**, 2462–2463 (2009).

28. S. G. Bucella, A. Luzio, E. Gann, L. Thomsen, C. R. McNeill, G. Pace, A. Perinot, Z. Chen, A. Facchetti, M. Caironi, Macroscopic and high-throughput printing of aligned nanostructured polymer semiconductors for MHz large-area electronics. *Nat. Commun.* **6**, 8394 (2015).

29. T. He, M. Stolte, C. Burschka, N. H. Hansen, T. Musiol, D. Kälblein, J. Pflaum, X. Tao, J. Brill, F. Würthner, Single-crystal field-effect transistors of new Cl$_2$-NDI polymorph processed by sublimation in air. *Nat. Commun.* **6**, 5954 (2015).

30. B. A. Jones, M. J. Ahrens, M.-H. Yoon, A. Facchetti, T. J. Marks, M. R. Wasielewski, High-mobility air-stable n-type semiconductors with processing versatility: Dicyanoperylene-3,4:9,10-bis(dicarboximides). *Angew. Chem. Int. Ed. Engl.* **43**, 6363–6366 (2004).

31. J. Soeda, T. Uemura, Y. Mizuno, A. Nakao, Y. Nakazawa, A. Facchetti, J. Takeya, High electron mobility in air for *N,N'*-1*H*,1*H*-perfluorobutyldicyanoperylene carboxydi-imide solution-crystallized thin-film transistors on hydrophobic surfaces. *Adv. Mater.* **23**, 3681–3685 (2011).

32. I. Vladimirov, M. Kellermeier, T. Gessner, Z. Molla, S. Grigorian, U. Pietsch, L. S. Schaffroth, M. Küehn, F. May, R. T. Weitz, High-mobility, ultrathin organic semiconducting films realized by surface-mediated crystallization. *Nano Lett.* **18**, 9–14 (2018).

33. Q. Miao, Ten years of N-heteropentacenes as semiconductors for organic thin-film transistors. *Adv. Mater.* **26**, 5541–5549 (2014).

34. M. V. Gorelik, S. P. Titovia, M. A. Kanor, Reaction of α-halogeno- and α-nitroanthraquinones with the anions of CH acids. Part 1. Synthesis of 1-alkyl-, 1,5-dialkyl-, and 1-aroylanthraquinones. *J. Org. Chem. USSR* **28**, 1852–1857 (1992).

35. M. V. Gorelik, S. P. Titovia, M. A. Kanor, Reaction of α-halogeno- and a-nitroanthraquinones with the anions of CH acids. Part 2. Peri-cyclization in the reaction with nitriles. *J. Org. Chem. USSR* **28**, 1858–1864 (1992).

36. H. Konishi, T. Sekino, K. Manabe, Palladium-catalyzed external-CO-free carbonylation of aryl bromides using 2,4,6-trichlorophenyl formate. *Chem. Pharm. Bull.* **66**, 562–567 (2018).

37. T. Steiner, The hydrogen bond in the solid state. *Angew. Chem. Int. Ed.* **41**, 48–76 (2002).

38. U. Zschieschang, K. Amsharov, M. Jansen, K. Kern, H. Klauk, R. T. Weitz, Separating the impact of oxygen and water on the long-term stability of n-channel perylene diimide thin-film transistors. *Org. Electron.* **26**, 340–344 (2015).

39. The parasitic effect and extrinsic factors such as grain boundaries can be neglected.

40. T. Uemura, Y. Hirose, M. Uno, K. Takimiya, J. Takeya, Very high mobility in solution-processed organic thin-film transistors of highly ordered [1]benzothieno[3,2-b]benzothiophene derivatives. *Appl. Phys. Express* **2**, 111501 (2009).

41. H. H. Choi, K. Cho, C. D. Frisbie, H. Sirringhaus, V. Podzorov, Critical assessment of charge mobility extraction in FETs. *Nat. Mater.* **17**, 2–7 (2017).

42. K. Lee, É. D. Murray, L. Kong, B. I. Lundqvist, D. C. Langreth, Higher-accuracy van der Waals density functional. *Phys. Rev. B* **82**, 081101 (2010).

43. S. Fratini, S. Ciuchi, D. Mayou, G. T. de Laissardière, A. Troisi, A map of high-mobility molecular semiconductors. *Nat. Mater.* **16**, 998–1002 (2017).

44. To determine the cause of this behavior and to solve the problem, a study of the annealing condition for the device is underway in our laboratory.

45. J. Soeda, T. Uemura, T. Okamoto, C. Mitsui, M. Yamagishi, J. Takeya, Inch-size solution-processed single-crystalline films of high-mobility organic semiconductors. *Appl. Phys. Express* **6**, 076503 (2013).

46. J. Soeda, T. Okamoto, C. Mitsui, J. Takeya, Stable growth of large-area single crystalline thin films from an organic semiconductor/polymer blend solution for high-mobility organic field-effect transistors. *Org. Electron.* **39**, 127–132 (2016).

47. S. Kumagai, A. Yamamura, T. Makita, J. Tsurumi, Y. Y. Lim, T. Wakimoto, N. Isahaya, H. Nozawa, K. Sato, M. Mitani, T. Okamoto, S. Watanabe, J. Takeya, Scalable fabrication of organic single-crystalline wafers for reproducible TFT arrays. *Sci. Rep.* **9**, 15897 (2019).

48. G. W. T. M. J. Frisch, H. B. Schlegel, G. E. Scuseria, M. A. Robb, J. R. Cheeseman, G. Scalmani, V. Barone, B. Mennucci, G. A. Petersson, H. Nakatsuji, M. Caricato, X. Li, H. P. Hratchian, A. F. Izmaylov, J. Bloino, G. Zheng, J. L. Sonnenberg, M. Hada, M. Ehara, K. Toyota, R. Fukuda, J. Hasegawa, M. Ishida, T. Nakajima, Y. Honda, O. Kitao, H. Nakai, T. Vreven, J. A. Montgomery, J. J. E. Peralta, F. Ogliaro, M. Bearpark, J. J. Heyd, E. Brothers, K. N. Kudin, V. N. Staroverov, T. Keith, R. Kobayashi, J. Normand, K. Raghavachari, A. Rendell, J. C. Burant, S. S. Iyengar, J. Tomasi, M. Cossi, N. Rega, J. M. Millam, M. Klene, J. E. Knox, J. B. Cross, V. Bakken, C. Adamo, J. Jaramillo, R. Gomperts, R. E. Stratmann, O. Yazyev, A. J. Austin, R. Cammi, C. Pomelli, J. W. Ochterski, R. L. Martin, K. Morokuma, V. G. Zakrzewski, G. A. Voth, P. Salvador, J. J. Dannenberg, S. Dapprich, A. D. Daniels, O. Farkas, J. B. Foresman, J. V. Ortiz, J. Cioslowski, D. J. Fox, *Gaussian 09, Revision D. 01* (Gaussian Inc., 2013).

49. S. F. Boys, F. Bernardi, The calculation of small molecular interactions by the differences of separate total energies. Some procedures with reduced errors. *Mol. Phys.* **19**, 553–566 (1970).

50. M. W. Schmidt, K. K. Baldridge, J. A. Boatz, S. T. Elbert, M. S. Gordon, J. H. Jensen, S. Koseki, N. Matsunaga, K. A. Nguyen, S. Su, T. L. Windus, M. Dupuis, J. A. Montgomery Jr, General atomic and molecular electronic structure system. *J. Comput. Chem.* **14**, 1347–1363 (1993).

51. S. Sakai, J. Soeda, R. Häusermann, H. Matsui, C. Mitsui, T. Okamoto, M. Ito, K. Hirose, T. Sekiguchi, T. Abe, M. Uno, J. Takeya, All solution-processed organic single-crystal transistors with high mobility and low-voltage operation. *Org. Electron.* **22**, 1–4 (2015).

52. J. Wang, R. M. Wolf, J. W. Caldwell, P. A. Kollman, D. A. Case, Development and testing of a general amber force field. *J. Comput. Chem.* **25**, 1157–1174 (2004).

53. C. I. Bayly, P. Cieplak, W. Cornell, P. A. Kollman, A well-behaved electrostatic potential based method using charge restraints for deriving atomic charges: the RESP model. *J. Phys. Chem.* **97**, 10269–10280 (1993).

54. H. J. C. Berendsen, J. P. M. Postma, W. F. van Gunsteren, A. DiNola, J. R. Haak, Molecular dynamics with coupling to an external bath. *J. Chem. Phys.* **81**, 3684–3690 (1984).

55. S. Nosé, A molecular dynamics method for simulations in the canonical ensemble. *Mol. Phys.* **52**, 255–268 (1984).

56. S. Nosé, A unified formulation of the constant temperature molecular dynamics methods. *J. Chem. Phys.* **81**, 511–519 (1984).

57. W. G. Hoover, Canonical dynamics: Equilibrium phase-space distributions. *Phys. Rev. A* **31**, 1695–1697 (1985).

58. M. Parrinello, A. Rahman, Polymorphic transitions in single crystals: A new molecular dynamics method. *J. Appl. Phys.* **52**, 7182–7190 (1981).

59. B. Hess, H. Bekker, H. J. C. Berendsen, J. G. E. M. Fraaije, LINCS: A linear constraint solver for molecular simulations. *J. Comput. Chem.* **18**, 1463–1472 (1997).

60. T. Darden, D. York, L. Pedersen, Particle mesh Ewald: An $N{\cdot}\log(N)$ method for Ewald sums in large systems. *J. Chem. Phys.* **98**, 10089–10092 (1993).

61. H. Horinouchi, H. Sakai, Y. Araki, T. Sakanoue, T. Takenobu, T. Wada, N. V. Tkachenko, T. Hasobe, Controllable electronic structures and photoinduced processes of bay-linked perylenediimide dimers and a ferrocene-linked triad. *Chem. Eur. J.* **22**, 9631–9641 (2016).

62. J. Mizuguchi, Phase change of N, N'-Bis (2-phenylethyl)perylene-3, 4:9, 10-bis (dicarboximide) for information storage applications. *Mol. Cryst. Liq. Cryst.* **322**, 291–298 (1998).

63. T. Uemura, C. Rolin, T.-H. Ke, P. Fesenko, J. Genoe, P. Heremans, J. Takeya, On the extraction of charge carrier mobility in high-mobility organic transistors. *Adv. Mater.* **28**, 151–155 (2016).

64. M.-M. Ling, P. Erk, M. Gomez, M. Koenemann, J. Locklin, Z. Bao, Air-stable n-channel organic semiconductors based on perylene diimide derivatives without strong electron withdrawing groups. *Adv. Mater.* **19**, 1123–1127 (2007).

65. B. A. Jones, A. Facchetti, M. R. Wasielewski, T. J. Marks, Effects of arylene diimide thin film growth conditions on n-channel OFET performance. *Adv. Funct. Mater.* **18**, 1329–1339 (2008).